

The LSST-DESC 3x2pt Tomography Optimization Challenge

JOE ZUNTZ,¹ FRAN OIS LANUSSE,² ALEX I. MALZ,³ ANGUS H. WRIGHT,⁴ AN ZE SLOSAR,⁵ BELA ABOLFATHI,⁶ DAVID ALONSO,⁷ ABBY BAULT,⁶ CL CIO R. BOM,^{8,9} MASSIMO BRESCIA,¹⁰ ADAM BROUSSARD,¹¹ JEAN-ERIC CAMPAGNE,¹² STEFANO CAVUOTI,^{10,13,14} EDUARDO S. CYPRIANO,¹⁵ BERNARDO M. O. FRAGA,⁸ ERIC GAWISER,¹¹ ELIZABETH J. GONZALEZ,^{8,16,17} DYLAN GREEN,⁶ PETER HATFIELD,¹⁸ KARTHEIK IYER,¹⁹ DAVID KIRKBY,⁶ ANDRINA NICOLA,²⁰ ERFAN NOURBAKHSH,²¹ ANDY PARK,⁶ GABRIEL TEIXEIRA,⁸ KATRIN HEITMANN,²² EVE KOVACS,²² YAO-YUAN MAO,²³ AND THE LSST DARK ENERGY SCIENCE COLLABORATION (LSST DESC)

¹ Institute for Astronomy, University of Edinburgh, Edinburgh EH9 3HJ, United Kingdom

² AIM, CEA, CNRS, Universit  Paris-Saclay, Universit  Paris Diderot, Sorbonne Paris Cit , F-91191 Gif-sur-Yvette, France

³ German Centre of Cosmological Lensing, Ruhr-Universit t, Universit tsstra e 150, 44801 Bochum, Germany

⁴ Ruhr University Bochum, Faculty of Physics and Astronomy, Astronomical Institute (AIRUB), German Centre for Cosmological Lensing, 44780 Bochum, Germany

⁵ Brookhaven National Laboratory, Upton NY 11973, USA

⁶ Department of Physics and Astronomy, University of California, Irvine, CA 92697, USA

⁷ Astrophysics, University of Oxford, DWB, Keble Road, Oxford OX1 3RH, UK

⁸ Centro Brasileiro de Pesquisas F sicas, Rua Dr. Xavier Sigaud 150, 22290-180 Rio de Janeiro, RJ, Brazil

⁹ Centro Federal de Educa o Tecnol gica Celso Suckow da Fonseca, Rodovia M rcio Covas, lote J2, quadra J - Itagua  (Brazil)

¹⁰ INAF - Osservatorio Astronomico di Capodimonte, via Moiariello 16, I-80131, Napoli Italy

¹¹ Department of Physics and Astronomy, Rutgers, the State University, Piscataway, NJ 08854, USA

¹² Universit  Paris-Saclay, CNRS/IN2P3, IJCLab, 91405 Orsay, France

¹³ INFN - Sezione di Napoli, via Cinthia 21, I-80126 Napoli, Italy

¹⁴ Department of Physics "E. Pancini", University of Naples Federico II, via Cintia, 21, I-80126 Napoli, Italy

¹⁵ Universidade de S o Paulo, IAG, Rua do Mat o 1225, S o Paulo, SP, Brazil

¹⁶ Instituto de Astronom a Te rica y Experimental (IATE-CONICET), Laprida 854, X5000BGR, C rdoba, Argentina.

¹⁷ Observatorio Astron mico de C rdoba, Universidad Nacional de C rdoba, Laprida 854, X5000BGR, C rdoba, Argentina.

¹⁸ Astrophysics, University of Oxford, Denys Wilkinson Building, Keble Road, Oxford, OX1 3RH, UK

¹⁹ Dunlap Institute for Astronomy and Astrophysics, University of Toronto, 50 St George St, Toronto, ON M5S 3H4, Canada

²⁰ Department of Astrophysical Sciences, Princeton University, Peyton Hall, Princeton, NJ 08544, USA

²¹ Department of Physics and Astronomy, University of California, Davis, Davis, CA 95616, USA

²² Argonne National Laboratory, 9700 S Cass Ave, Lemont, IL 60439, USA

²³ Department of Physics and Astronomy, Rutgers University, Piscataway, NJ 08854, USA

ABSTRACT

This paper presents the results of the Rubin Observatory Dark Energy Science Collaboration (DESC) 3x2pt tomography challenge, which served as a first step toward optimizing the tomographic binning strategy for the main DESC analysis. The task of choosing an optimal tomographic binning scheme for a photometric survey is made particularly delicate in the context of a metacalibrated lensing catalogue, as only the photometry from the bands included in the metacalibration process (usually *riz* and potentially *g*) can be used in sample definition. The goal of the challenge was to collect and compare bin assignment strategies under various metrics of a standard 3x2pt cosmology analysis in a highly idealized setting to establish a baseline for realistically complex follow-up studies; in this preliminary study, we used two sets of cosmological simulations of galaxy redshifts and photometry under a simple noise model neglecting photometric outliers and variation in observing conditions, and contributed algorithms were provided with a representative and complete training set. We review and evaluate the entries to the challenge, finding that even from this limited photometry information, multiple algorithms can separate tomographic bins reasonably well, reaching figures-of-merit scores close to the attainable maximum. We further find that adding the *g* band to *riz* photometry improves metric performance by $\sim 15\%$ and that the optimal bin assignment strategy depends strongly on the science case: which figure-of-merit is to be optimized, and which observables (clustering, lensing, or both) are included.

Keywords: methods: statistical – dark energy – large-scale structure of the universe

1. INTRODUCTION

Weak gravitational lensing (WL) has emerged over the last decade as a powerful cosmological probe (Heymans et al. 2012; Hildebrandt et al. 2016; Troxel et al. 2018; Asgari et al. 2021; Hamana et al. 2020). WL uses measurements of coherent shear distortion to the observed shapes of galaxies to track the evolution of large-scale gravitational fields. It measures the integrated gravitational potential along lines of sight to source galaxies, and can thence constrain the laws of gravity, the expansion history of the Universe, and the history and growth of cosmic structure.

WL has proven especially powerful in combination with galaxy clustering measurements, which can measure the density of matter up to an unknown bias function. The high signal to noise of such measurements and the relative certainty of the redshift of these foreground samples breaks degeneracies in the systematic errors that affect WL.

The $3\times 2pt$ method has become a standard tool for performing this combination. In this method, two-point correlations are computed among and between two samples, the shapes of background (source) galaxies and the locations of foreground (lens) galaxies, which trace foreground dark matter haloes. The three combinations (source-source, source-lens, and lens-lens) are measured in either Fourier or configuration space, and can be predicted from a combination of perturbation theory and simulation results. The method has been used in the Dark Energy Survey, DES, (Abbott et al. 2018), and to combine the Kilo-Degree Survey, KiDS with spectroscopic surveys (Heymans et al. 2021; van Uitert et al. 2018; Joudaki et al. 2018).

Most lensing and $3\times 2pt$ analyses have chosen to analyze data *tomographically*, binning galaxies by redshift. This approach captures almost all the available information in lensing data, since lensing measures an integrated effect and so galaxies nearby in redshift probe very similar fields. For photometric foreground samples, tomography also loses little information when reasonably narrow bins are used, since redshift estimates of such galaxies have large uncertainties¹. Binning galaxies by approximate redshift also lets us model galaxy bias, intrinsic alignments, and other systematic errors en masse in a more tractable way. While fully 3D meth-

ods have been proposed, prototyped, and shown to have significant promise, (Heavens 2003; Kitching et al. 2015), the tomographic approach remains the standard within the field. Tomographic $3\times 2pt$ measurements will be a key science goal in the upcoming *Stage IV* surveys, including the Vera C. Rubin Observatory (Ivezic et al. 2019) and the Euclid and Roman space telescopes (Lau reijs et al. 2011; Akeson et al. 2019).

We are free to assign galaxies to different tomographic bins in any way we wish; changing the choice can potentially affect the ease with which we can calibrate the bins, but any choice can lead to correct cosmology results. The bins need not even be assigned contiguous redshift ranges: we can happily correlate bins with multiple redshifts if that is useful, or by some other galaxy property than redshift entirely. We should choose, then, an assignment algorithm that maximises the constraining power for a science case of interest. This challenge explores such algorithms.

Various recent work have explored general tomographic binning strategies. The general question of optimization was recently discussed in detail in Kitching et al. (2019) using a self-organizing map (SOM) approach to target up to five tomographic bins. For this configuration they find that equally spaced redshift bins are a good proxy for an optimized method, but note, importantly, that we should not be constrained to trying to directly match our bin selections to specific tomographic bin edges. They also highlight the utility of rejecting outlier or hard-to-classify objects from samples, and the ability of SOMs to do so cleanly. Taylor et al. (2018b) considered using fine tomographic bins as an alternative to fully 3D lensing, and found that the strategy of equal numbers per bin is less effective at high redshift, a result we will echo in this paper. The fine-binning strategy also allows a set of nulling methods to be applied, offering various advantages in avoiding poorly-understood regimes (Taylor et al. 2018a; Bernardeau et al. 2014; Taylor et al. 2021).

This paper is part of preparations for the analysis to be run by the Dark Energy Science Collaboration (DESC) of Legacy Survey of Space and Time (LSST) data from the Rubin Observatory. In it, we discuss and evaluate the related challenge of using a limited set of colour bands to make those assignments, motivated by requirements of using the metacalibration method for galaxy shape measurement to limit biases. A similar question, with different motivations, was explored in Jain et al. (2007), who found that 3-band *gri* tomography could be

¹ Spectroscopic foreground samples may be more likely to see significant gains from moving beyond tomographic methods.

effective for tomographic selection, a result we will echo here in a new context: in this paper we describe the results of a challenge using simulated Rubin-like data with a range of methods submitted by different teams. We explore how many tomographic bins we can effectively generate using only a subset of bands, and compare methods submitted to the challenge.

In section 2 we explain the need for methods that work on limited sets of bands in the context of upcoming lensing surveys. In section 3 we describe the design of the challenge and the simulated data used in it. Section 4 briefly describes the entrants to the challenge, and discusses their performance (full method details are given in appendix B). We conclude in section 5.

2. MOTIVATION

The methodology used to assign galaxies to bins faces special challenges when we use a particularly effective approach for measuring galaxy shear, called *metacalibration* (metacal), which was introduced in Sheldon & Huff (2017) and developed further in Sheldon et al. (2020). In metacal, galaxy images are deconvolved from the point-spread function (PSF), sheared, and reconolved before measurement, allowing one to directly compute the response of a metric to underlying shear and correct for it when computing two-point measurements. This can almost completely remove errors due to model and estimator (noise) bias from WL data, at least when PSFs are well-measured and oversampled by the pixel grid. The method has been successfully applied in the DES Year 1 and Year 3 analyses (Zuntz et al. 2018; Gatti et al. 2020), and application to early Rubin data is planned.

Furthermore, metacal provides a solution to the pernicious and general problem of *selection biases* in WL. Measurements of galaxy shear are known to have noise-induced errors that are highly covariant with those on other galaxy properties, including size and, most importantly, flux and magnitude. It follows that a cut (or re-weighting) on galaxy magnitudes, or on any quantity derived from them, will induce a shear bias since galaxies will preferentially fall on either side of the cut depending on their shear. Within metacal, we can compute and thus account for this bias very accurately, by performing the cut on both sheared variants of the catalogue, and measuring the difference between the post-cut shear in the two variants. In DES the corrected biases were found up to around 4%, far larger than the requirements for the current generation of surveys (Zuntz et al. 2018).

In summary: metacal allows us to correct for significant selection biases, but only if all selections are performed using only bands in which the PSF is measured

well enough for deconvolution to be performed². For Rubin, this means using only the r , i , z , and perhaps g bands. In this work we therefore study how well we can perform tomography using only this limited photometric information. In particular, this limitation prevents us from using the most obvious method for tomography, and computing a complete photometric redshift probability density function (PDF) for each galaxy and assigning a bin using the mean or peak of that PDF³.

Simulation methods can also be used to correct for selection biases, provided that they match the real data to high accuracy. If we determine that limiting the bands we can use for tomography results in a significant decrease in our overall 3x2pt signal-to-noise, outweighing the gain from the improved shape calibration then this might suggest moving to rely more on such methods⁴. Constructing simulations with the required fidelity is challenging at Rubin-level accuracy and requires careful comparison to deep field data.

3. CHALLENGE DESIGN

The DESC Tomographic Challenge opened in May 2020 and accepted entries until September 2020.

In the challenge, participants assigned simulated galaxies to tomographic bins, using only their (g)riz bands and associated errors, and the galaxy size. Their goal was to maximize the cosmological information in the final split data set; this is generally achieved by separating different bins by redshift as much as possible. Participants were free to optimize or simply select nominal (target) redshift bin edges from their training sample, but in either case had to assign galaxies into the different bins.

This meant there were two ways to obtain higher scores: either to improve the choice of nominal bin edges, or to find better ways to assign objects to those bins. This was a sub-optimal design decision: separating the two issues would have enabled us to more easily delineate the advantages of different methods. This can be explored retrospectively, since we know what approach methods took, but would have been easier in advance.

² Alternative or extended methods to the metacalibration process described here, modelling the full likelihood space of deconvolved galaxy properties in a unified way might one day be feasible, but are likely to be computationally challenging.

³ This only prevents us using other photometry for *selection*, not for *characterization* after objects have been selected, such as computing the overall number density $n(z)$ for a tomographic bin.

⁴ One can account for residual shear estimation uncertainty during parameter estimation by marginalizing over an unknown factor. Widening the prior on this factor decreases the overall constraining power of the analysis.

This and other mistakes in designing the challenge are described in [Appendix C](#).

This differs from many redshift estimation questions because we are not at all concerned with estimates of individual galaxy redshifts; instead, this challenge was designed as a classification and bin-optimization problem, amenable to more direct machine-learning methods. As such we used the training / validation / testing approach, as standard in machine-learning analyses. The determination of the $n(z)$ of the recovered bins (whether with per-galaxy estimates or otherwise) was not part of the challenge.

3.1. *Philosophy*

Since this was a preliminary challenge designed to explore whether it is possible *in theory* to use only the (g)riz bands for tomography, we chose to simplify several aspects of the data. In realistic situations we will have access to limited sized training sets for WL photometric redshifts, since spectra are time-consuming to obtain. These training sets will also be highly incomplete compared to full catalogues, especially at faint magnitudes where spectroscopic coverage is sparse. In this challenge we avoided both these issues – the training samples we provided (see [subsection 3.2](#)) were comparable in size to the testing sample, and drawn from the same population. Given this, the challenge represents a best-case scenario – if no method succeeded on this easier case then more realistic cases would probably be impossible.

Despite these simplifications, the other aspects of the challenge and process were designed to be as directly relevant as possible to the particular WL science case we focus on. The data set was chosen to mimic the population, noise, and cuts we will use in real data (see [subsubsection 3.2.3](#)) and the metrics were designed to be as close to the science goals as possible, rather than a lower level representation (see [subsection 3.3](#)). The data set was also large enough to pose a reasonably realistic test of methods at the large data volume required for upcoming surveys, where $10^9 - 10^{10}$ galaxies will be measured.

The challenge was open to any entrants, not just those already involved in DESC, but it was advertised through Rubin channels, and so is perhaps best described as semi-public. Participants developed and tested their methods locally but submitted code to be run as part of a central combined analysis at the National Energy Research Supercomputing Center (NERSC), where the final tests and metric evaluation were conducted. No prize was offered apart from recognition.

3.2. *Data*

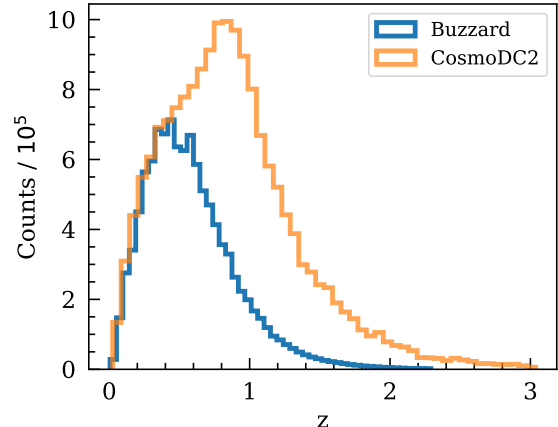


Figure 1. The underlying redshift number density $n(z)$ for the two catalogues used in the challenge, after the initial cuts described in the text.

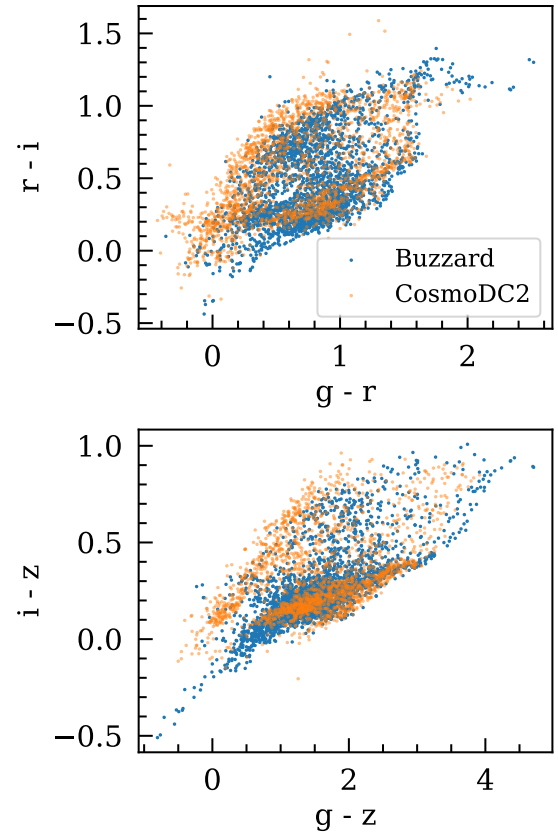


Figure 2. Colour-colour diagrams for the two catalogues used in the challenge, showing the bands available to participants.

We ran challenge entries on two data sets, CosmoDC2 and Buzzard, each of which is split into training, validation, and testing components. In each case participants were supplied with the training and validation data, and

the testing data was kept secret for final evaluation. In each case the three data sets were random sub-selections of the full data sets, with the training and testing sets 25% of the full data each and the validation 50%.

Using two catalogues allows us to check for over-fitting in the design of models themselves, and thus to determine whether two reasonable but different galaxy populations can be optimized by the same methods; this will tell us whether our conclusions might be reasonable for real data. We discuss correlations between metric scores on the two data sets in Section 4.4.

Each of these data sets come from cosmological simulations which provide truth values of galaxy magnitudes and sizes. We simulate and add noise to the objects as described below.

3.2.1. *CosmoDC2*

The CosmoDC2 simulation was designed to support DESC and is described in detail in Korytov et al. (2019). It covers 440 deg² of sky, and used the dark matter particles from the Outer Rim simulations (Heitmann et al. 2019). The UniverseMachine (Behroozi et al. 2019) simulations were then used, with the GalSampler technique (Hearin et al. 2020), in a combination of empirical and semi-analytic methods, to assign galaxies with a limited set of specified properties to halos.

These objects were then matched to outputs of the Galacticus model (Benson 2012), which generated complete galaxy properties and which was run on an additional DESC simulation, AlphaQ, and included all the LSST bands. The simulation is complete to $r = 28$, and contains objects up to redshift 3. We include the ultra-faint galaxies, not assigned to a specific halo, in our sample.

One limitation of the CosmoDC2 catalogues, found as part of the challenge, was that the matching to Galacticus led to only a limited number of SEDs being used at high redshifts, and thus too many galaxies in the simulations sharing similar characteristics at these redshifts, such as colour-colour relations. It was unknown whether this limitation would have any practical impact on the challenge; this was a reason for adopting the additional Buzzard catalogue.

3.2.2. *Buzzard*

The Buzzard catalogue was developed to support the DES Year 1 (DES-Y1) data analysis, and is described in detail in DeRose et al. (2019). It has previously been used in DESC analyses, for example in Schmidt et al. (2020a). The catalogue used dark matter simulations from L-GADGET2 Springel (2005) and then added galaxies using an algorithm that matches a set of galaxy property probability densities to data using

sub-halo abundance matching. Buzzard galaxies extend to around redshift 2.3 (significantly shallower than CosmoDC2) and were shown to be a good match (after appropriate selections) to DES-Y1 observable catalogues. Magnitudes using the LSST band passes were provided in the catalogue.

3.2.3. *Post-processing*

We add noise to the truth values in the extra-galactic catalogues to simulate real observations. In each case we simulate first year Rubin observations using the DESC TXPIPE framework⁵, following the methodology of Ivezić et al. (2010) and assuming the numerical values for telescope and sky characteristics therein.

In both simulations we add two cuts to approximately simulate the selection used in a real lensing catalogue. In both cases we apply a cut on the combined riz signal to noise of $S/N > 10$, and a size cut $T/T_{\text{psf}} > 0.5$, where T is the trace $I_{xx} + I_{yy}$ of the moments matrix and measures the squared (deconvolved) radius of the galaxy, and T_{psf} is a fixed Rubin PSF size of 0.75 arc-seconds.

After this section, and cuts to contiguous geographic regions, we used around 20M objects from the Buzzard simulations and around 36M objects from the CosmoDC2 simulations. The nominal 25% training data sets were therefore 5M and 9M objects respectively, but many entrants trained their methods on a reduced subset of the data. To make training tractable but consistent for the full suite we therefore trained all methods with 1M objects for each data set.

The overall number density $n(z)$ of the two data sets is shown in Figure 1, and a set of colour-colour diagrams in Figure 2.

3.3. *Metrics*

In this challenge we use only a lensing source (background) population, since the metacal requirements do not apply to the foreground lens sample. We do, however, calculate 3x2pt metrics using the same source and lens populations, both because this scenario is one that will be used in some analyses, and because clustering-like statistics of lensing samples are important for studies of intrinsic alignments. We use three different sets of metrics, one based on the overall signal to noise of the angular power spectra derived from the samples, and two based on a figure-of-merit for the constraints that would be obtained using them. The relationships between these metrics in our results are discussed in subsection 4.4. We compute each metric on three different sets of summary statistics: lensing-alone, clustering-

⁵ <https://github.com/LSSTDESC/TXPIPE>

alone, and the full 3x2pt. We therefore compute a total of nine values for each bin selection.

For each bin i generated by a challenge entry, we make a histogram of the true redshifts of each galaxy assigned to the bin. This is then used as our number density $n_i(z)$ in the metrics below. Both metrics reward bins that can cleanly separate galaxies by redshift, since this reduces the covariance between the samples. No method can perfectly separate them, so good methods reduce the tails of $n_i(z)$ that overlap with neighbouring bins.

We developed two implementations of each of these metrics, one using the Core Cosmology Library (Chisari et al. 2019) and one the JAX Cosmology Library (Lanusse & et al. 2021), which provides differentiable theory predictions using the JAX library (Bradbury et al. 2018). In production we use the latter since it provided a more stable calculation of metric 2.

Metric 1 would be approximately measurable on real data without performing a full cosmology analysis, whereas metrics 2 and 3 would be the final output of such an analysis. They therefore test performance at what would be multiple stages in the wider pipeline. In each case the metrics are constructed so that a larger value is a better score.

3.3.1. Metric 1: SNR

Our first metric is the total signal-to-noise ratio (SNR) of the power spectrum derived from the assigned $n_i(z)$ values:

$$S = \mu^T C^{-1} \mu \quad (1)$$

where μ is a stack of the theoretical predictions for the C_ℓ spectra for each tomographic bin, in turn, and C a estimate of the covariance between them, making the approximation that the underlying density field has a Gaussian distribution as described in Takada & Jain (2004) and summarized in Appendix A. We compute this metric for lensing alone, clustering alone, and the full 3x2pt combination.

3.3.2. Metrics 2 & 3: $w_0 - w_a$ and $\Omega_c - \sigma_8$ FOMs

Metric 2 uses a figure of merit (FOM) based on that presented by the Dark Energy Task Force (DETF) (Albrecht et al. 2006). We use the inverse area of a Fisher Matrix ellipse, which approximates the size in two axes of the posterior PDF one would obtain on analysing the spectra:

$$F = \left(\frac{\partial \mu}{\partial \theta} \right)^T C^{-1} \left(\frac{\partial \mu}{\partial \theta} \right), \quad (2)$$

$$\text{FOM} = \frac{1}{2\pi \sqrt{\det([F^{-1}]_{p_1, p_2})}} \quad (3)$$

where $[F^{-1}]_{p_1, p_2}$ extracts the 2x2 matrix for two parameters. We use both the original DETF variant in which $p_1 = w_0$ and $p_2 = w_a$, representing the constraining power on dark energy evolution, and a version in which $p_1 = \Omega_c$ and $p_2 = \sigma_8$, representing constraining power on overall cosmic structure amplitude (σ_8), and its evolution (a function of Ω_c). In each case the complete parameter space consists of the seven $w_0 w_a CDM$ cosmological parameters; we used the parameter combination used natively by the DESC core cosmology library (Chisari et al. 2019) ($\Omega_c, \Omega_b, H_0, \sigma_8, n_s, w_0, w_a$). This simplified measure does not include any nuisance parameters modelling systematic errors in the analysis (most importantly the galaxy bias parameters in the clustering spectra), and like all Fisher analyses approximates posterior constraints as Gaussian.

3.4. Infrastructure

The challenge was structured as a python library, in which each assignment method was a subclass of an abstract base parent superclass, TOMOGRAPHER. The superclass, and other challenge machinery, performed initialization, configuration option handling, data loading, and computing derived quantities such as colours from magnitudes.

Participants were expected to subclass TOMOGRAPHER and implement two methods, TRAIN and APPLY. Each was required to accept as an argument an array or dictionary of galaxy properties (magnitudes, and, optionally, sizes, errors, and colours). The TRAIN method was also passed an array of true redshift values, which could be used however they wished. Methods were submitted to the challenge in the form of a pull request to the challenge repository on GitHub⁶.

The training and validation parts of the data set were made available for training and hyper-parameter tuning. Once the challenge period was complete, the algorithms were collected from the pull requests and run at NERSC. If a method failed due to a difference in the runtime environment or the hardware at NERSC, the participants and organizers tried to amend it after the formal challenge period ended, though this was not always possible.

3.5. Control Methods

Two “control” methods were used to test the challenge machinery and ensure that metrics behaved appropriately in specific limits.

The RANDOM algorithm randomly assigned galaxies to each tomographic bin, resulting in bins which each

⁶ http://github.com/LSSTDESC/tomo_challenge

had the same $n(z)$, on average (the random noise fluctuations are very small when using this number of galaxies). Using this method, we expect that increasing the number of bins should not increase any metric score, since bins are maximally correlated. We find this to be true for all our metrics.

The IBANDONLY method used only the i -band to select tomographic bins, splitting galaxies in equal-sized bins in this magnitude. We expect only a small increase in metric score with the number of bins, and also that the addition of the g -band should make no difference to scores. Again, we find this to be true.

4. METHODS & RESULTS

Twenty-five methods were submitted to the challenge, including the control methods described above. Most used machine learning methods of various types to perform the primary classification, rather than trying to perform a full photometric redshift analysis. These methods are listed in Table 1 and described in full in Appendix B.

4.1. Result types

The methods described above were run on a data set, previously unseen by entrants but drawn from the same underlying population, of size 8.6M objects for CosmoDC2 (our fiducial simulation) and 5.4M objects for Buzzard. A complete suite of the metrics described in Section 3.3 was run on each of the two for each method. In total, each method was run on 16 scenarios, each combination of: $griz$ vs. riz , Buzzard vs. CosmoDC2, and 3, 5, 7, and 9 bins requested. Nine metrics were calculated for each scenario: clustering, lensing, and 3x2pt for each of the SNR metric (Equation 1), the $w_0 - w_a$ DETF FOM, and the $\Omega_c - \sigma_8$ FOM (Equation 3).

4.2. Results Overview

The DETF results for each method are shown in Table 2. Complete results for all metrics for the nine-bin scenario only are shown in appendix Tables 3 and Table 4.

In all these tables, missing entries are shown for two reasons. The first, marked with an asterisk, is when a method did not run for the given scenario, either due to memory overflow or taking an extremely long time. The second, marked with a dash, is when a method ran, but generated at least one bin with an extremely small number count, such that the spectrum could not be calculated.

No one method dominates the metrics across the different scenarios considered. Before the challenge began we somewhat arbitrarily chose the 9-bin 3x2pt $griz$ CosmoDC2 $w_0 - w_a$ metric as the fiducial scenario on which

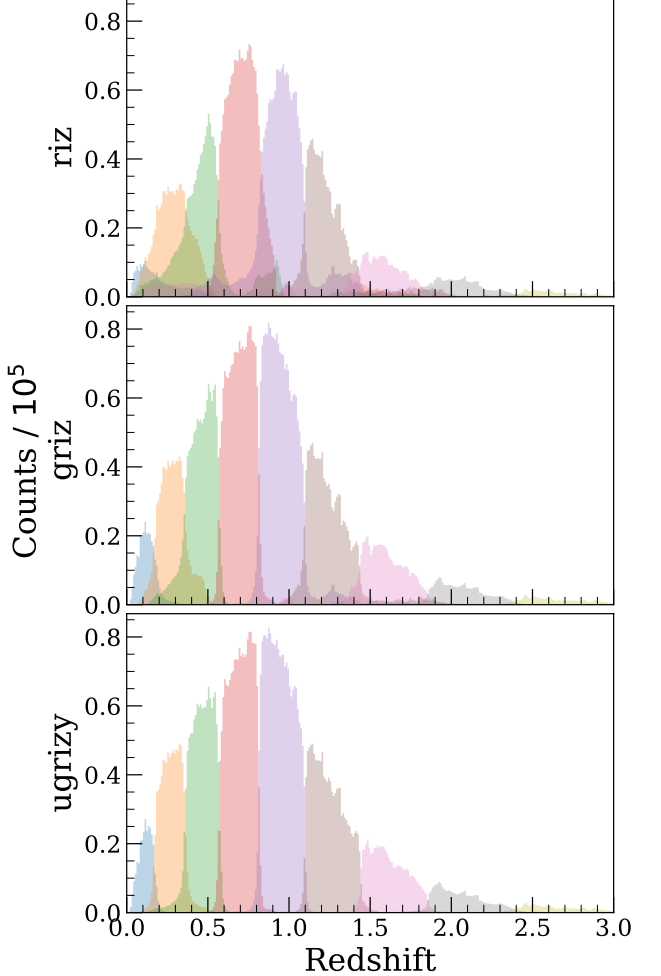


Figure 3. The tomographic $n(z)$ values generated by the winning method in the challenge, FUNBINS, generating nine bins with the CosmoDC2 data. The upper panel shows results for the method applied to riz bands, and the middle on $griz$. The lower panel is for comparison and is not part of the challenge; it illustrates FUNBINS results using all the $ugrizy$ bands. The increased spread and overlap of the bins as bands are removed decreases the overall constraining power and signal-to-noise.

an overall winning method would be selected. By this criterion the best method was, by a small margin, FUNBINS, which used a random forest to assign galaxies to after choosing nominal bin edges that split the range spanned by the sample into equal co-moving distance bins. As described in subsection B.17, this splitting was designed to minimize the shot noise for the angular power in each bin, and this has proven successful. Figure 3 shows the number density obtained by this method, for both the riz and $griz$ scenarios, and an additional post-challenge run using the full Rubin $ugrizy$ bands. The metrics FUNBINS obtained on $ugrizy$ are barely higher

Name	Description	Submitters
RANDOM	Random assignment (control method)	Organizers
IBANDONLY	i-band only (control method)	Organizers
RANDOMFOREST	A collection of individual decision trees	Organizers
LSTM	Long Short-Term Memory neural network	CRB, BF, GT, ESC, EJG
AUTOKERASLSTM ^a	Automatically configured LSTM variant.	CRB, BF, GT, ESC, EJG
LGBM	Light Gradient Boosted Machine	CRB, BF, GT, ESC, EJG
TCN	Temporal Convolution Network	CRB, BF, GT, ESC, EJG
CNN	Convolutional Neural Network	CRB, BF, GT, ESC, EJG
ENSEMBLE	Combination of three other network methods	CRB, BF, GT, ESC, EJG
SIMPLESOM	Self-Organizing Map	CRB, BF, GT, ESC, EJG
PQNLD	Extension of SIMPLESOM combining with template-based redshift estimation	AHW
UTOPIA	Nearest-neighbours, optimised in the limit of large representative training sets	AHW
COMPLEXSOM	Extension of SIMPLESOM with an additional assignment optimization	DA, AHW, AN, EG, BA, ABr
GPzBINNING	Gaussian Process redshift estimator and binner	PH
JAXCNN/JAXRESNET	Two related CNN-based bin edge optimizers	AP
NEURALNETWORK1/2	Dense network optimizing bin assignment for two metrics	FL
PCACLUSTER	Principal Component Analysis of fluxes then optimized clustering	DG
ZOTBIN/ZOTNET	Two related neural network methods with a preprocesing normalizing flow	DK
FFNN	Feed-forward neural network	EN
FUNBINS	Random forest with various nominal bin edge selection	ABA
MLPQNA	Multi-layer perceptron	SC, MB
STACKED GENERALIZATION	Combination of Gradient Boosted Trees classifiers with standard Random Forests (50/50)	JEC

Table 1. Methods entered into the challenge. The algorithms are described more fully in Appendix B.

^aA technical problem, involving conflicting versions of libraries and incompatible hardware, meant that AutoKerasLSTM could not be run in the final challenge.

than those with $griz$ – the largest increase is 8% for the $\Omega_c - \sigma_8$ metric, with the remainder all 5% or less.

Other methods performed better in other branches of the challenge; in particular we note ZOTNET, STACKED GENERALIZATION, and NEURALNETWORK (see sections B.16, B.20, and B.14 respectively), which each won more than three 9-bin scenarios. An illustration of the rank achieved by each method within each challenge configuration and for each metric is shown in Figure 4.

These results suggest that, at least in our idealised scenario of perfect training sets and given the limitations of our simulations, restricted photometry does not necessarily catastrophically limit our ability to use tomography. In both the CosmoDC2 and Buzzard data sets, even the riz bands alone are sufficient to split objects into nine reasonably separated tomographic bins. Once bins become this narrow the primary analysis concern will become the calibration of overall bin $n(z)$ values,

rather than initial tomography, so we consider this to be reassuring.

There is a clear widening of the $n(z)$ when losing the g -band. This widening leads to a loss in constraining power, which is discussed more in Section 4.5.

For comparison, we also show results using all six LSST bands, $ugrizy$; these could not be used with the metacalibration method. The improvement in the sharpness of the bins is noticeable but not large. We quantify this in Figure 5, which shows the fraction of objects that are in ambiguous redshift slices, defined as objects in redshift ranges where there are more objects assigned to another tomographic bin. The total fraction of such objects is also shown. This illustrates how adding the g band improves the assignment for almost every pair of bins, and reduce the ambiguous fraction by a factor of three to the point where a significant majority of galaxies are clearly assigned. Further adding the re-

Method	riz				griz			
	3-bin	5-bin	7-bin	9-bin	3-bin	5-bin	7-bin	9-bin
COMPLEXSOM	38.0	52.1	94.4	101.6	34.9	45.0	91.6	100.3
JAXCNN	59.9	101.9	105.2	—	79.7	125.2	150.0	—
JAXRESNET	73.7	111.1	131.6	—	82.2	126.0	—	161.5
NEURALNETWORK1	76.3	117.6	135.8	109.9	81.9	132.9	158.0	96.9
NEURALNETWORK2	30.5	48.0	57.8	136.1	49.4	102.7	122.2	140.0
PCACLUSTER	29.5	68.1	75.8	*	50.1	72.7	90.8	*
ZOTBIN	64.8	106.4	121.8	135.3	77.6	120.0	141.8	154.7
ZOTNET	73.6	111.2	131.8	145.9	83.7	128.5	150.1	167.2
AUTOKERAS_LSTM	31.1	74.9	103.4	—	44.1	67.5	122.2	98.4
CNN	27.1	50.8	76.7	103.3	30.5	57.7	95.4	122.4
ENSEMBLE1	65.6	65.6	94.8	*	*	*	*	*
FUNBINS	36.8	82.5	122.1	141.8	42.1	100.4	142.5	167.2
GPzBINNING	26.2	49.7	80.8	111.7	27.8	55.3	87.2	126.9
IBANDONLY	38.0	50.0	54.4	57.3	38.0	50.0	54.4	57.3
LGBM	27.0	50.8	78.8	108.2	30.3	57.4	92.9	125.2
LSTM	26.7	51.1	81.4	103.6	30.2	57.1	95.9	126.9
MLPQNA	39.3	64.7	93.2	121.8	42.8	72.2	109.0	133.7
STACKED GENERALIZATION	35.3	60.5	83.5	120.4	39.4	63.9	93.1	148.9
PQNLD	39.5	60.5	77.7	105.4	42.9	71.0	105.9	133.8
RANDOM	1.2	1.2	1.2	1.2	1.2	1.2	1.2	1.2
RANDOMFOREST	39.5	65.2	93.2	118.5	43.0	72.8	110.1	136.5
SIMPLESOM	39.5	59.9	77.9	98.5	42.2	73.2	108.0	134.8
FFNN	39.0	64.3	90.3	114.7	43.0	72.0	112.3	137.2
TCN	40.0	65.3	90.9	110.5	44.1	72.8	108.0	134.0
UTOPIA	39.0	63.7	90.8	112.2	43.1	74.0	112.8	139.3

Table 2. Values of the 3x2pt DETF (w_0, w_a) figure-of-merit achieved by entrant methods on the CosmoDC2 part of the challenge. The horizontal line separates two general approaches to the problem, as discussed in subsection 4.6: those below the line used fixed target edges for tomographic bins and optimized the assignment of objects to those bins, whereas those above also optimized the target edges themselves.

maining u and y bands improves the assignment in a way that is smaller, though not insignificant, in both relative and absolute terms. This latter addition also does not translate into large increases in the figures of merit: the DETF score for CosmoDC2 is 169.7, barely higher than its score of 167.2 for *griz*, and this is also true for other metrics. While this is only a general indication and not a thorough exploration, it is encouraging.

FUNBINS seems to be a good and stable general method, though several other methods perform as well or slightly better in other scenarios. Notably, many methods reach the same plateau in lensing-only metrics, suggesting this is somewhat easier to optimize; this is consistent with the general reason that photometric redshifts suffice for lensing: the broad lensing kernels are less sensitive to small changes.

Several of the neural network methods perform well up to seven tomographic bins but fail when run with nine. This is presumably not an intrinsic feature of

these methods, but depends on implementation details. Further development solving these challenges should be valuable, since they are among the highest scoring seven-bin methods.

4.3. Non-assignment

The challenge did not require entrants to assign all galaxies to bins; aside from the impact of reduced final sample size on the metrics, no additional penalty was applied for discarding galaxies entirely. Several methods took advantage of this. The ComplexSom method (see subsection B.10) found it did not improve scores, but as noted in subsection B.9 this may be an artifact of

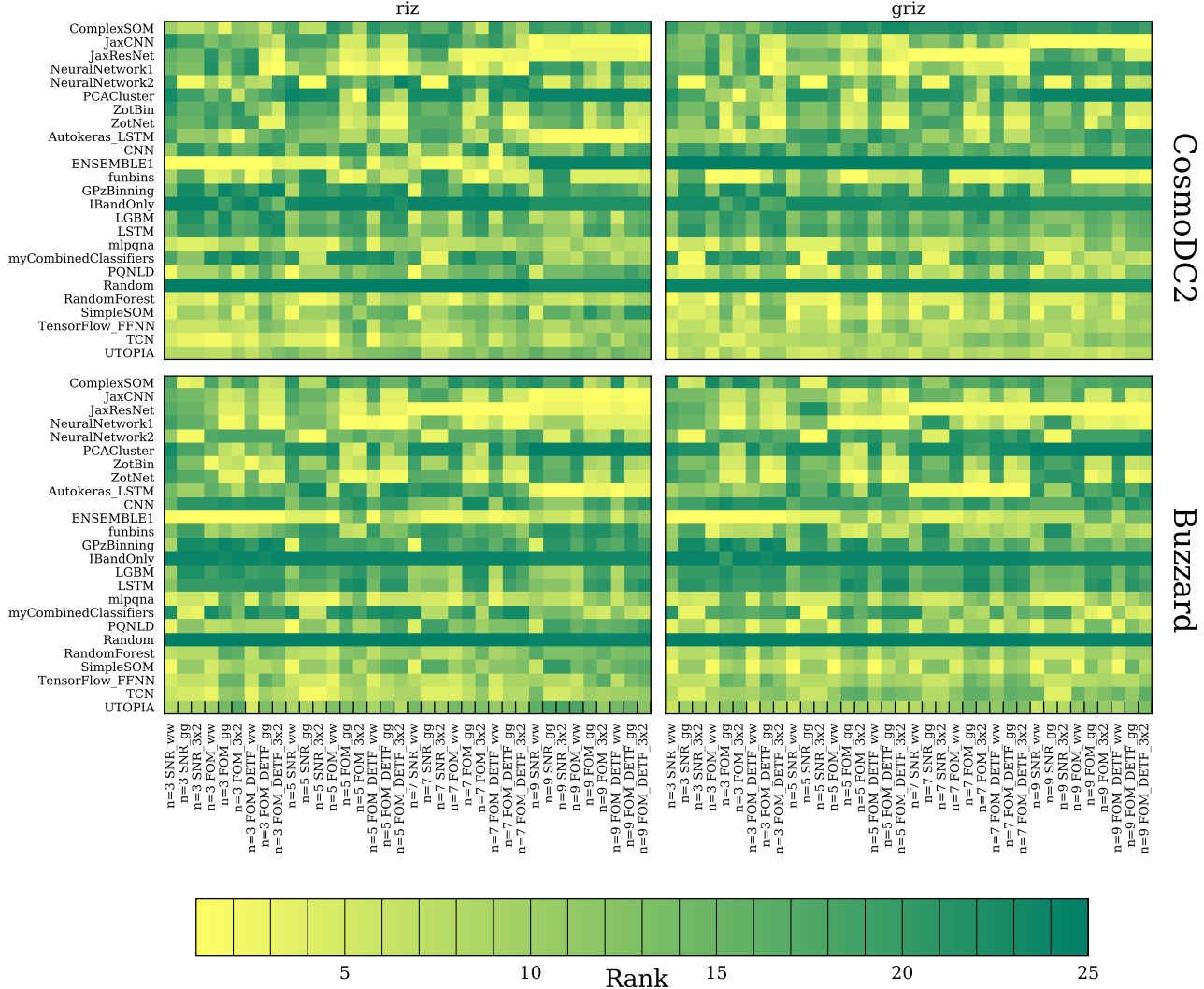


Figure 4. The rank of each method (1 = highest scoring, 25 = lowest scoring) within each configuration of the challenge, for each metric separately. A method that was good everywhere would appear as yellow strip across an entire horizontal range.

the high density of the training data, and so could be explored in future challenges⁷.

4.4. Metric comparisons

Figure 6 shows a comparison of some of the different metrics used in the challenge. We plot, using assignments for methods and for all bin counts, the relation-

ship between our fiducial metric, the DETF 3x2pt on CosmoDC2, and other metrics we measured.

The different metrics are generally well-correlated (this also holds true for the metrics not shown here), especially at the highest values of the metrics representing the most successful methods. This is particularly so when comparing the Buzzard and CosmoDC2 metrics, which is encouraging as it implies these methods are broadly stable to reasonable changes in the underlying galaxy distribution, and hence on the survey properties. The largest outlier comes from the NEURAL NETWORK entry.

⁷ In real data or more realistic simulations discarding galaxies has more complicated effects than simply decreasing sample size as it does here - removing objects with broad $p(z)$ can narrow the final $n(z)$, not just lower it. This was not a factor in this challenge because we use true redshifts to calculate our metrics.

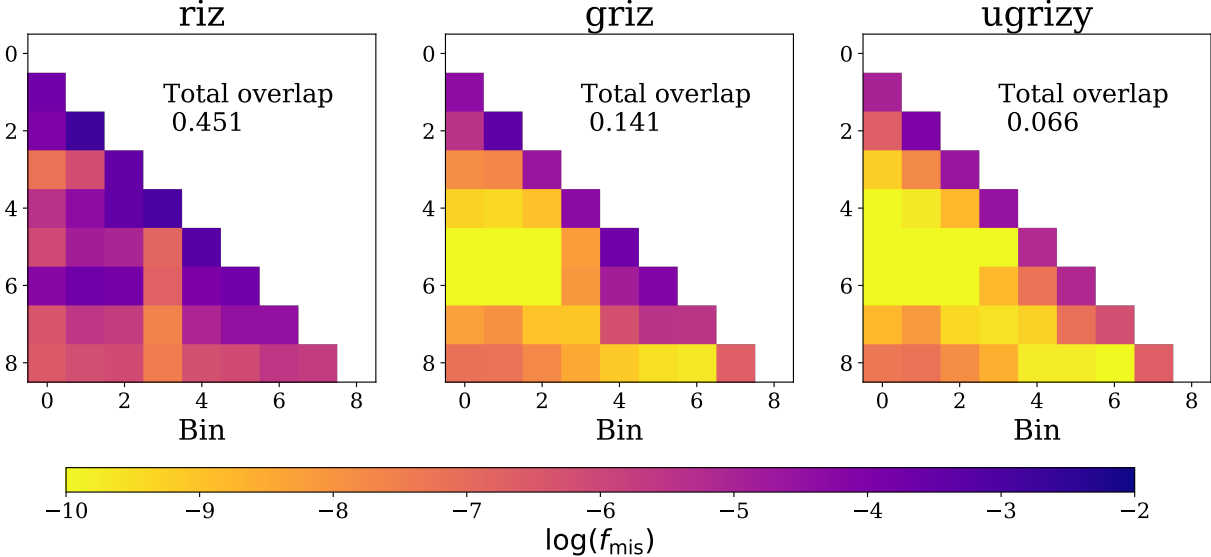


Figure 5. The pairwise fractions f_{mis} of total objects in redshift regions where multiple tomographic bins contain galaxies, for the FUNBINS tomography method and three choices of bands. The x - and y -axes show tomographic bin indices, and the colour represents the fraction of objects (compared to the total number in the challenge) that are at redshifts where both tomographic bins have members, in bins of width $\delta z = 10^{-3}$. This metric corresponds to the fraction of the area that is shaded in two colours in Figure 3. The total-overlap figure gives the total fraction of objects that are ambiguous over all bins, and is the sum of all the pairwise values.

This is not true of the overall winning method for large bin counts - as shown in the tables in Appendix E, significantly more methods achieve a top-scoring spot in the Buzzard table 4 than in the CosmoDC2 table 3. This reinforces the conclusion discussed below in subsection 4.6 that target bin edges should be re-optimized for each new scenario, though the relatively noisy results make this difficult to interpret.

The relatively broader spread in the lensing-only metric illustrates how our metric is dominated by the stronger constraining power in the clustering part of the data set. This arises because we do not include a galaxy bias model in our FOM, and so the constraining power of the clustering is artificially high; this limitation is one reason we explore a wide variety of metrics.

Finally, there is a bimodal structure in the relationship between the FOM and SNR metrics. This largely traces the split between models which train the target bin edges vs those which fix them, as described below in Section 4.6.

4.5. Impact of losing g -band

Figure 7 shows the ratio of the FOM between methods using the griz and the same method using the riz. Each point represents one method with a specific number of bins, indicated by colour. For lower scoring methods and for smaller numbers of bins there is more scatter in the ratio, but for the highest scoring algorithms and con-

figurations the loss when losing g -band is a little more stable, at around 10–15%.

The value of the extra FoM that could be gained should be weighed against the challenge of high-accuracy PSF measurement for this band, and the cost in time and effort of determining it, but until the end of the survey this is unlikely to be the limiting factor in overall precision.

4.6. Trained edges vs fixed edges

Some of the methods in the challenge accepted target bin edges as an input to their algorithms, and then used classifiers to assign objects to those bins. Entrants could select these edges; many followed the example random forest entry and split into equal counts per bin. Other methods optimized the values of bin edges themselves, by maximizing a metric. For the runs shown here, these methods mostly targeted one of the 3x2pt metrics.

A comparison of trained-edge and fixed-edge methods on the CosmoDC2 griz scenarios is shown in Figure 8, and the same data normalized against the score achieved by objects binned in true redshift (i.e. a perfect assignment method) are shown in Figure 9.

One important point to note is that while trained-edge methods dominate the highest scores for the 3x2pt DETF metric, on which they trained, they fare much worse on the lensing-only metrics (the methods were not re-trained on the lensing metrics; we show the metrics for the same assigned bins). This suggests that the dif-

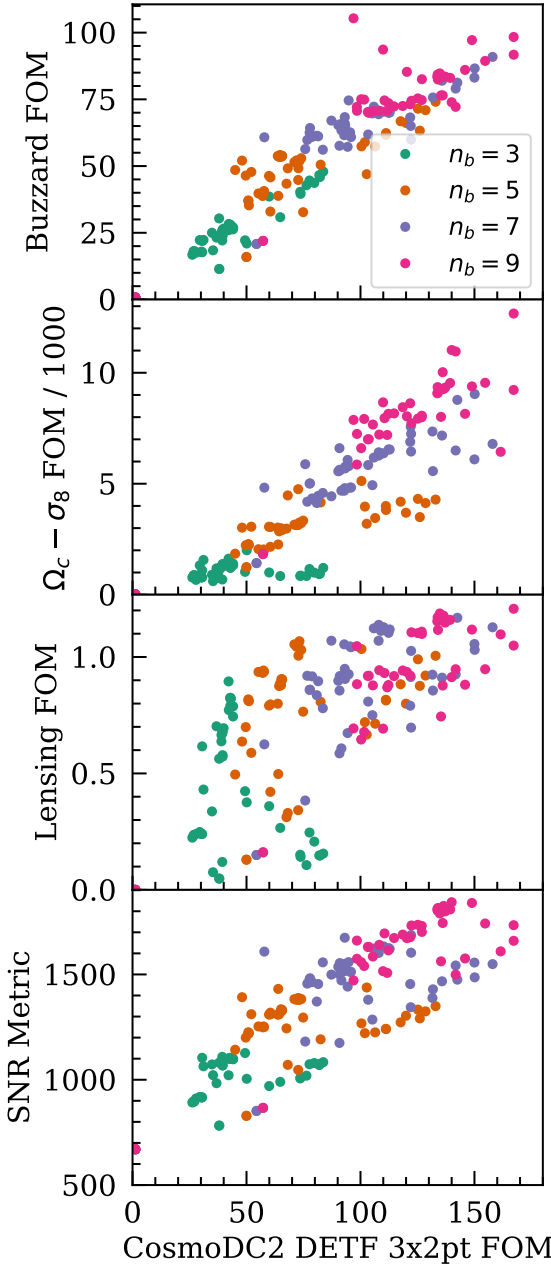


Figure 6. A comparison of the metrics used in our challenge for the different methods that were entered. The x-axis is shared, and shows the 3x2pt $w_0 - w_a$ (DETF) figure of merit on the CosmoDC2 data set for all methods, with colours labelling the number of bins used. Each of the panels shows a metric which is the same except for a single change, which is labelled on its y-axis. For example, the top panel still shows the 3x2pt $w_0 - w_a$ (DETF) figure of merit, but for the Buzzard data set.

ference between optimal bins for different science cases is a significant one, and thus that analysis pipelines should make it straightforward to calibrate multiple configurations and pass them to subsequent science analysis; this will probably be true even when comparing models differing only in their systematic parametrizations. This feature is highlighted by the comparison between the two variants of the NEURALNETWORK entry, which differed only in which metric they were targeting; optimizing one metric does not optimize the other (though the changes between results on the two simulations could also indicate that this is related to the high-redshift behaviour in the CosmoDC2 simulation described in 3.2.1).

Among methods with fixed bins, those using equal numbers in each tend to plateau at scores of 120–140 in Table 2, suggesting that a range of machine learning models can effectively classify by bin, at least in this case of representative, extensive training information. Notably, this is the case even for the UTOPIA entry, which uses the nearest training set neighbour to assign bins and thus is explicitly optimised for this idealised scenario; it should give an upper limit when using the same fixed bins. That other methods with the same nominal bin choice achieve scores close to it once again confirms that many entries are close to the best possible score for this approach.

Several of the methods with optimized target bin edges break this barrier and achieve very high scores. This included ZotNet, ZotBin, and JaxResNet. The Stacked Generalization method similarly included manually tuned bin edges to maximize score for this scenario (and indeed its ensemble combination method could be applied to combine the other successful methods). The typical 15–20% improvement in FoM scores when optimizing nominal bin edges makes clear that re-selecting edges for each science case is worth the time and effort required.

Notably, though, the winning CosmoDC2 FUNBINS method used the simpler approach described above. The success of this simple and fast solution suggests this as an easy heuristic for well-optimized nominal edges, at least for cases where clustering-like metrics are important. Its relatively lower scores on the Buzzard metrics, as noted in subsection 4.4, does however further highlight the importance of science- and sample-specific training.

5. CONCLUSIONS

The Tomography Challenge has proved a useful mechanism for encouraging the development of methods for this science question. We encourage this challenge structure for other well-specified science cases, and DESC has

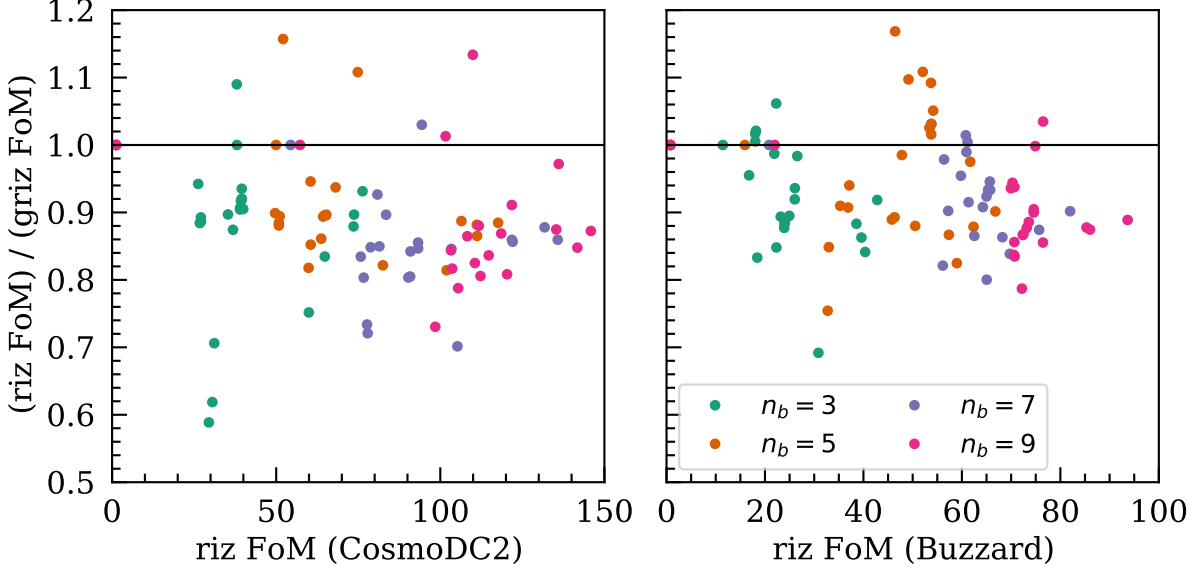


Figure 7. The degradation in constraining power over all methods including and excluding the g-band, in terms of the ratio of the $w_0 - w_a$ figure of merit. The left-hand panel shows results for the CosmoDC2 scenarios, and the right-hand panel for the Buzzard scenarios. Colours indicate the number of bins used in the analysis. Some methods perform worse when adding the g-band and have ratios greater than unity.

subsequently run other challenges along the same lines such as the N5K beyond-limber challenge⁸. We describe in Appendix C some lessons we have learned from this challenge that may be useful for future ones.

The results of the challenge have shown that three or four-band photometry is sufficient for specifying tomography even up to a large number of bins, if the training data is complete enough: degeneracies between colour do not make this impossible. Excluding the g-band from the data reduces the constraining power by a noticeable but not catastrophic amount ($\sim 15\%$).

The wide range in scores for nominally similar methods (for example, the several methods using neural network approaches) reminds us that, generically, the implementation details of machine learning methods can drastically affect their performance.

Finally, we have shown that in general there is a significant advantage to optimizing target bins afresh when considering a new science case; this can be a significant boost to the final constraining power. Despite this, evenly spaced bins in fiducial co-moving distance have proven a good general choice, as shown in the winning method in the challenge, FUNBINS.

The challenge was heavily simplified, with the intention of testing whether effective bin-assignments with limited photometry is possible even in theory, and of

generating as many potential methods for the task as possible. With both these achieved, future directions for simulating the problem are clear. The most obvious is limited spectroscopic completeness and size. Realistic training data sets will be far smaller than the millions of objects we used here, and the difficulty of measuring spectra for faint galaxies will make them incomplete and highly unrepresentative. Machine learning methods will be particularly affected by the latter problem. Future challenges must explore these important limitations using simulated incompleteness, and use realistic photo-z methods to compute metrics.

6. ACKNOWLEDGEMENTS

This paper has undergone internal review in the LSST Dark Energy Science Collaboration. The internal reviewers were Markus Michael Rau, Christopher Morrison, and Shahab Joudaki.

AHW is supported by a European Research Council Consolidator Grant (No. 770935). The work of EG and ABr was supported by the U.S. Department of Energy, Office of Science, Office of High Energy Physics Cosmic Frontier Research program under Award Number DE-SC0010008. CRB, ESC, BMOF, EJG, and GT made use of multi-GPU Sci-Mind Brunelleschi machines developed and tested for Artificial Intelligence and would like to thank CBPF Multi GPU development team of LITCOMP/COTEC, for supporting this infrastructure. ESC acknowledges support from the FAPESP (#2019/19687-2) and CNPq (#308539/2018-

⁸ <https://github.com/LSSTDESC/N5K>

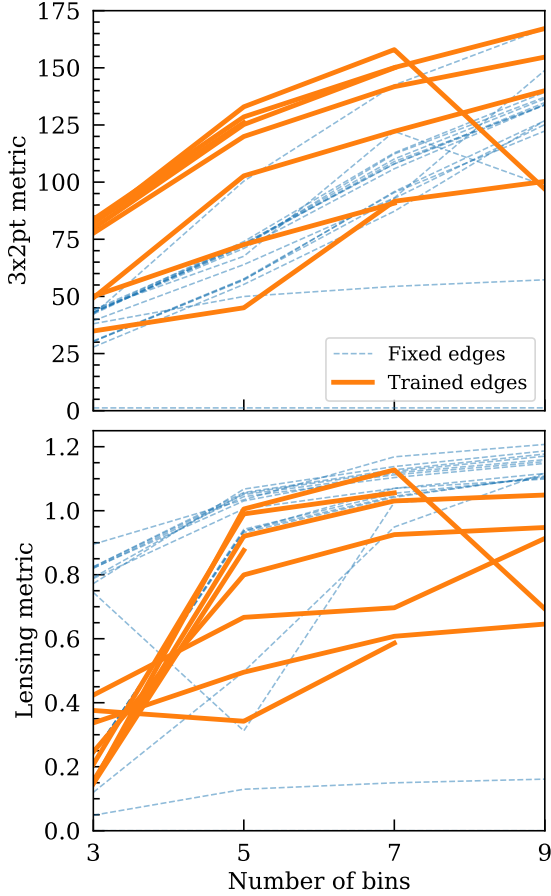


Figure 8. A comparison of results from methods which used fixed target edges (dashed blue) with those which optimized target bins (solid orange). Methods were trained on the 3x2pt metric shown in the upper panel; the lower performance for these classifications for the lensing-only metric shown in the lower panel illustrates the need for science case-specific binning choices. In each case, classification is done using griz bands on the CosmoDC2 data set.

4). MB acknowledges financial contributions from the

agreement ASI/INAF 2018-23-HH.0, Euclid ESA mission - Phase D. PH acknowledges generous support from the Hintze Family Charitable Foundation through the Oxford Hintze Centre for Astrophysical Surveys.

The DESC acknowledges ongoing support from the Institut National de Physique Nucléaire et de Physique des Particules in France; the Science & Technology Facilities Council in the United Kingdom; and the Department of Energy, the National Science Foundation, and the LSST Corporation in the United States. DESC uses resources of the IN2P3 Computing Center (CC-IN2P3–Lyon/Villeurbanne - France) funded by the Centre National de la Recherche Scientifique; the National Energy Research Scientific Computing Center, a DOE Office of Science User Facility supported by the Office of Science of the U.S. Department of Energy under Contract No. DE-AC02-05CH11231; STFC DiRAC HPC Facilities, funded by UK BIS National E-infrastructure capital grants; and the UK particle physics grid, supported by the GridPP Collaboration. This work was performed in part under DOE Contract DE-AC02-76SF00515

6.1. Author Contributions

Zuntz led the project, ran the challenge, wrote most paper text, and made plots. Lanusse submitted methods, made plots, and contributed to metrics, infrastructure, analysis, and conclusions. Malz and Wright made plots, and contributed to analysis and conclusions; Wright also submitted methods. Slosar submitted methods, wrote initial infrastructure, and assisted with challenge design. Authors Abolfathi to Teixeira submitted methods to the challenge. Subsequent authors generated the data used in the challenge and contributed to infrastructure used in the project.

Authors CRB, ESC, BMOF, EJG, and GT are collaborators from outside the Dark Energy Science Collaboration included here under a DESC publication policy exemption.

REFERENCES

Abbott, T. M. C., Abdalla, F. B., Alarcon, A., et al. 2018, *PhRvD*, 98, 043526, doi: [10.1103/PhysRevD.98.043526](https://doi.org/10.1103/PhysRevD.98.043526)

Akeson, R., Armus, L., Bachelet, E., et al. 2019, arXiv e-prints, arXiv:1902.05569. <https://arxiv.org/abs/1902.05569>

Albrecht, A., Bernstein, G., Cahn, R., et al. 2006, arXiv e-prints, astro. <https://arxiv.org/abs/astro-ph/0609591>

Almosallam, I. A., Jarvis, M. J., & Roberts, S. J. 2016a, *MNRAS*, 462, 726, doi: [10.1093/mnras/stw1618](https://doi.org/10.1093/mnras/stw1618)

Almosallam, I. A., Lindsay, S. N., Jarvis, M. J., & Roberts, S. J. 2016b, *MNRAS*, 455, 2387, doi: [10.1093/mnras/stv2425](https://doi.org/10.1093/mnras/stv2425)

Asgari, M., Lin, C.-A., Joachimi, B., et al. 2021, *A&A*, 645, A104, doi: [10.1051/0004-6361/202039070](https://doi.org/10.1051/0004-6361/202039070)

Bai, S., Kolter, J. Z., & Vladlen, K. 2018, arXiv preprint arXiv:1803.01271v2

Behroozi, P., Wechsler, R. H., Hearn, A. P., & Conroy, C. 2019, *MNRAS*, 488, 3143, doi: [10.1093/mnras/stz1182](https://doi.org/10.1093/mnras/stz1182)

Benítez, N. 2000, *ApJ*, 536, 571, doi: [10.1086/308947](https://doi.org/10.1086/308947)

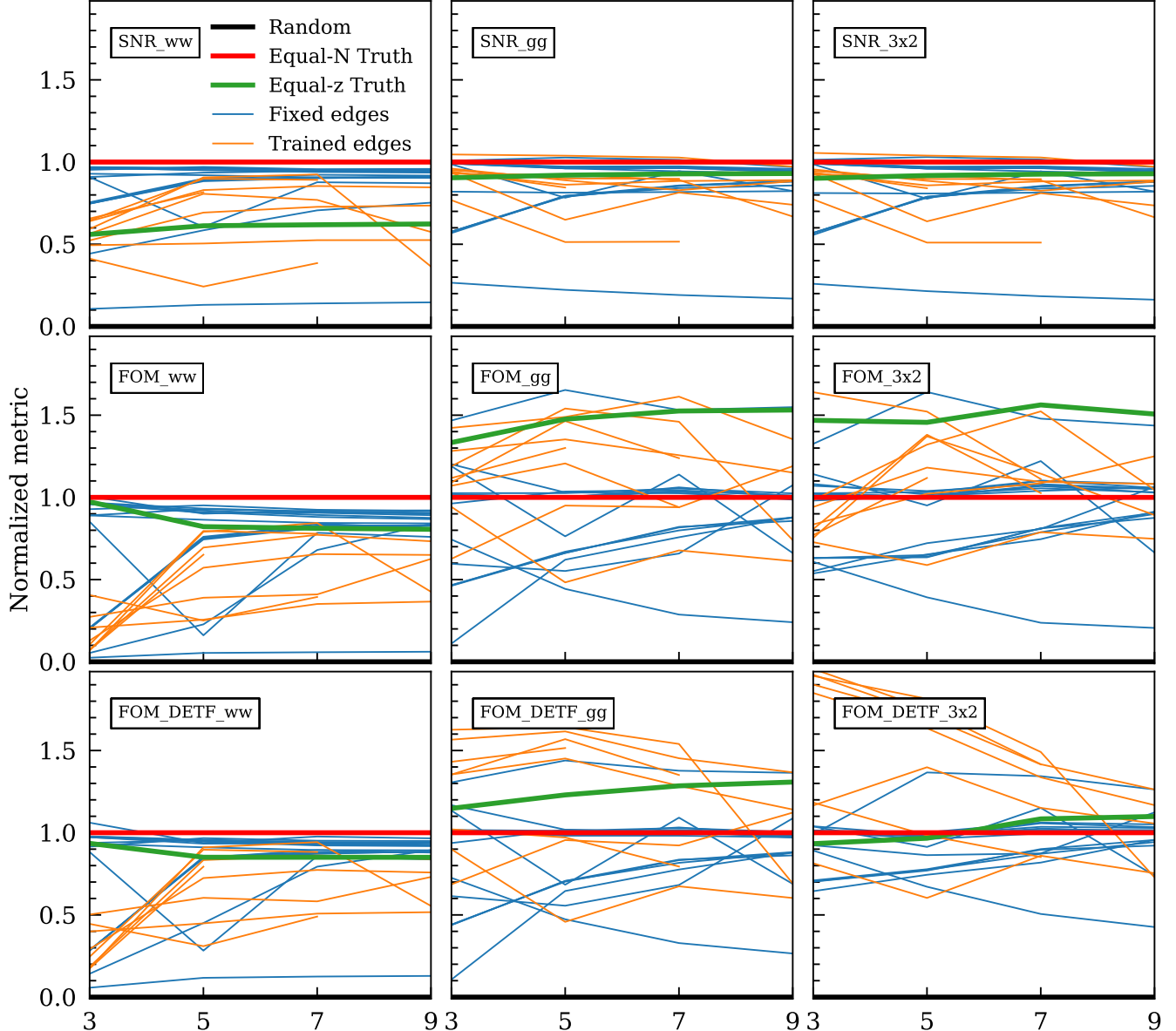


Figure 9. Normalized scores for each method, normalized between the score for random assignment (zero) and truth assignment to bins with equal number counts (one). It can be seen that both equal-number and equal-redshift spacings can be beaten for certain metrics. In each case, classification is done using griz bands on the CosmoDC2 data set; equivalent plots for Buzzard and riz are shown in Appendix D.

Benson, A. J. 2012, *NewA*, 17, 175,
doi: [10.1016/j.newast.2011.07.004](https://doi.org/10.1016/j.newast.2011.07.004)

Bernardeau, F., Nishimichi, T., & Taruya, A. 2014,
MNRAS, 445, 1526, doi: [10.1093/mnras/stu1861](https://doi.org/10.1093/mnras/stu1861)

Bottou, L., & Bengio, Y. 1995, in *Advances in Neural Information Processing Systems*, ed. G. Tesauro, D. Touretzky, & T. Leen, Vol. 7 (MIT Press), 585–592.
<https://proceedings.neurips.cc/paper/1994/file/a1140a3d0df1c81e24ae954d935e8926-Paper.pdf>

Bradbury, J., Frostig, R., Hawkins, P., et al. 2018, *JAX: composable transformations of Python+NumPy programs*, 0.1.77. <http://github.com/google/jax>

Breiman, L. 2001, *Machine Learning*, 45, 5,
doi: [10.1023/A:1010933404324](https://doi.org/10.1023/A:1010933404324)

Brescia, M., Cavuoti, S., Paolillo, M., Longo, G., & Puzia, T. 2012, *MNRAS*, 421, 1155,
doi: [10.1111/j.1365-2966.2011.20375.x](https://doi.org/10.1111/j.1365-2966.2011.20375.x)

Broussard, A., & Gawiser, E. 2021, Submitted to *ApJ*

Capak, P. L. 2004, PhD thesis, UNIVERSITY OF HAWAII

Cavuoti, S., Amaro, V., Brescia, M., et al. 2016, Monthly Notices of the Royal Astronomical Society, 465, 1959, doi: [10.1093/mnras/stw2930](https://doi.org/10.1093/mnras/stw2930)

Chisari, N. E., Alonso, D., Krause, E., et al. 2019, ApJS, 242, 2, doi: [10.3847/1538-4365/ab1658](https://doi.org/10.3847/1538-4365/ab1658)

Dauphin, Y. N., Fan, A., Auli, M., & Grangier, D. 2017, in International Conference on Machine Learning

de Boer, P.-T., Kroese, D., Mannor, S., & Rubinstein, R. Y. 2005, Annals of Operations Research, 134, 19

DeRose, J., Wechsler, R. H., Becker, M. R., et al. 2019, arXiv e-prints, arXiv:1901.02401. <https://arxiv.org/abs/1901.02401>

Duncan, K. J., Brown, M. J. I., Williams, W. L., et al. 2018, MNRAS, 473, 2655, doi: [10.1093/mnras/stx2536](https://doi.org/10.1093/mnras/stx2536)

Friedman, J. H. 2002, Comput. Stat. Data Anal., 38, 367, doi: [10.1016/S0167-9473\(01\)00065-2](https://doi.org/10.1016/S0167-9473(01)00065-2)

Gatti, M., Sheldon, E., Amon, A., et al. 2020, arXiv e-prints, arXiv:2011.03408. <https://arxiv.org/abs/2011.03408>

Gomes, Z., Jarvis, M. J., Almosallam, I. A., & Roberts, S. J. 2018, MNRAS, 475, 331, doi: [10.1093/mnras/stx3187](https://doi.org/10.1093/mnras/stx3187)

Hamana, T., Shirasaki, M., Miyazaki, S., et al. 2020, PASJ, 72, 16, doi: [10.1093/pasj/psz138](https://doi.org/10.1093/pasj/psz138)

Hastie, T., Tibshirani, R., & Friedman, J. 2009, The Elements of Statistical Learning (Springer, New York)

Hatfield, P. W., Almosallam, I. A., Jarvis, M. J., et al. 2020, MNRAS, 498, 5498, doi: [10.1093/mnras/staa2741](https://doi.org/10.1093/mnras/staa2741)

He, K., Zhang, X., Ren, S., & Sun, J. 2016, in 2016 IEEE Conference on Computer Vision and Pattern Recognition (CVPR), 770–778, doi: [10.1109/CVPR.2016.90](https://doi.org/10.1109/CVPR.2016.90)

Hearin, A., Korytov, D., Kovacs, E., et al. 2020, MNRAS, 495, 5040, doi: [10.1093/mnras/staa1495](https://doi.org/10.1093/mnras/staa1495)

Heavens, A. 2003, Monthly Notices of the Royal Astronomical Society, 343, 1327, doi: [10.1046/j.1365-8711.2003.06780.x](https://doi.org/10.1046/j.1365-8711.2003.06780.x)

Heek, J., Levskaya, A., Oliver, A., et al. 2020, Flax: A neural network library and ecosystem for JAX, 0.3.2. [http://github.com/google/flax](https://github.com/google/flax)

Heitmann, K., Finkel, H., Pope, A., et al. 2019, ApJS, 245, 16, doi: [10.3847/1538-4365/ab4da1](https://doi.org/10.3847/1538-4365/ab4da1)

Heymans, C., van Waerbeke, L., Miller, L., et al. 2012, Monthly Notices of the Royal Astronomical Society, 427, 146, doi: [10.1111/j.1365-2966.2012.21952.x](https://doi.org/10.1111/j.1365-2966.2012.21952.x)

Heymans, C., Tröster, T., Asgari, M., et al. 2021, A&A, 646, A140, doi: [10.1051/0004-6361/202039063](https://doi.org/10.1051/0004-6361/202039063)

Hildebrandt, H., Choi, A., Heymans, C., et al. 2016, MNRAS, 463, 635, doi: [10.1093/mnras/stw2013](https://doi.org/10.1093/mnras/stw2013)

Ivezic, Z., Jones, L., & Lupton, R. 2010, The LSST Photon Rates and SNR Calculations, v1.2, Tech. rep., LSST. http://faculty.washington.edu/ivezic/Teaching/Astr511/LSST_SNRdoc.pdf

Ivezic, Ž., Kahn, S. M., Tyson, J. A., et al. 2019, ApJ, 873, 111, doi: [10.3847/1538-4357/ab042c](https://doi.org/10.3847/1538-4357/ab042c)

Jain, B., Connolly, A., & Takada, M. 2007, Journal of Cosmology and Astroparticle Physics, 2007, 013, doi: [10.1088/1475-7516/2007/03/013](https://doi.org/10.1088/1475-7516/2007/03/013)

Jin, H., Song, Q., & Hu, X. 2019, in Proceedings of the 25th ACM SIGKDD International Conference on Knowledge Discovery & Data Mining, ACM, 1946–1956

Jolliffe, I. T., & Cadima, J. 2016, Philosophical Transactions of the Royal Society A: Mathematical, Physical and Engineering Sciences, 374, 20150202, doi: [10.1098/rsta.2015.0202](https://doi.org/10.1098/rsta.2015.0202)

Joudaki, S., Blake, C., Johnson, A., et al. 2018, MNRAS, 474, 4894, doi: [10.1093/mnras/stx2820](https://doi.org/10.1093/mnras/stx2820)

Ke, G., Meng, Q., Finley, T., et al. 2017, in Advances in Neural Information Processing Systems, ed. I. Guyon, U. V. Luxburg, S. Bengio, H. Wallach, R. Fergus, S. Vishwanathan, & R. Garnett, Vol. 30 (Curran Associates, Inc.), 3146–3154. <https://proceedings.neurips.cc/paper/2017/file/6449f44a102fde848669bdd9eb6b76fa-Paper.pdf>

Kingma, D. P., & Ba, J. 2014, arXiv e-prints, arXiv:1412.6980. <https://arxiv.org/abs/1412.6980>

Kitching, T. D., Heavens, A. F., & Das, S. 2015, MNRAS, 449, 2205, doi: [10.1093/mnras/stv193](https://doi.org/10.1093/mnras/stv193)

Kitching, T. D., Taylor, P. L., Capak, P., Masters, D., & Hoekstra, H. 2019, Phys. Rev. D, 99, 063536, doi: [10.1103/PhysRevD.99.063536](https://doi.org/10.1103/PhysRevD.99.063536)

Kohonen, T. 1982, Biological Cybernetics, 43, 59, doi: [10.1007/BF00337288](https://doi.org/10.1007/BF00337288)

Korytov, D., Hearin, A., Kovacs, E., et al. 2019, ApJS, 245, 26, doi: [10.3847/1538-4365/ab510c](https://doi.org/10.3847/1538-4365/ab510c)

Lanusse, F., & et al. 2021, In prep.

Laureijs, R., Amiaux, J., Arduini, S., et al. 2011, arXiv e-prints, arXiv:1110.3193. <https://arxiv.org/abs/1110.3193>

LeCun, Y., Bengio, Y., & Hinton, G. 2015, nature, 521, 436

Long, J., Shelhamer, E., & Darrell, T. 2015, in IEEE conference on computer vision and pattern recognition, 3431–3440

Medsker, L., & Jain, L. C. 1999, Recurrent neural networks: design and applications (CRC press)

Nocedal, J. 1980, Mathematics of Computation, 35, 773. <http://www.jstor.org/stable/2006193>

Papamakarios, G., Nalisnick, E., Jimenez Rezende, D., Mohamed, S., & Lakshminarayanan, B. 2019, arXiv e-prints, arXiv:1912.02762.
<https://arxiv.org/abs/1912.02762>

Pascanu, R., Mikolov, T., & Bengio, Y. 2013, in International conference on machine learning, 1310–1318

Pedregosa, F., Varoquaux, G., Gramfort, A., et al. 2011, Journal of Machine Learning Research, 12, 2825

Peng, H., & Bai, X. 2019, Astrodynamics, 3, doi: [10.1007/s42064-018-0055-4](https://doi.org/10.1007/s42064-018-0055-4)

Planck Collaboration, Ade, P. A. R., Aghanim, N., et al. 2016, A&A, 594, A13, doi: [10.1051/0004-6361/201525830](https://doi.org/10.1051/0004-6361/201525830)

Powell, M. J. D. 1964, The Computer Journal, 7, 155, doi: [10.1093/comjnl/7.2.155](https://doi.org/10.1093/comjnl/7.2.155)

R Core Team. 2015, R: A Language and Environment for Statistical Computing, R Foundation for Statistical Computing, Vienna, Austria.
<https://www.R-project.org/>

Raichoor, A., Mei, S., Erben, T., et al. 2014, ApJ, 797, 102, doi: [10.1088/0004-637X/797/2/102](https://doi.org/10.1088/0004-637X/797/2/102)

Rasmussen, C. E., & Williams, C. K. I. 2005, Gaussian Processes for Machine Learning (Adaptive Computation and Machine Learning) (The MIT Press)

Remy, P. 2020, Temporal Convolutional Networks for Keras, <https://github.com/philipperemy/keras-tcn>, GitHub

Rosenblatt, F. 1961, Principles of Neurodynamics: Perceptrons and the Theory of Brain Mechanisms (Springer, Berlin, Heidelberg)

Schmidt, S. J., Malz, A. I., Soo, J. Y. H., et al. 2020a, Monthly Notices of the Royal Astronomical Society, 499, 1587, doi: [10.1093/mnras/staa2799](https://doi.org/10.1093/mnras/staa2799)

—. 2020b, Monthly Notices of the Royal Astronomical Society, 499, 1587, doi: [10.1093/mnras/staa2799](https://doi.org/10.1093/mnras/staa2799)

Schuster, M., & Paliwal, K. K. 1997, IEEE transactions on Signal Processing, 45, 2673

Sheldon, E. S., Becker, M. R., MacCrann, N., & Jarvis, M. 2020, ApJ, 902, 138, doi: [10.3847/1538-4357/abb595](https://doi.org/10.3847/1538-4357/abb595)

Sheldon, E. S., & Huff, E. M. 2017, ApJ, 841, 24, doi: [10.3847/1538-4357/aa704b](https://doi.org/10.3847/1538-4357/aa704b)

Springel, V. 2005, MNRAS, 364, 1105, doi: [10.1111/j.1365-2966.2005.09655.x](https://doi.org/10.1111/j.1365-2966.2005.09655.x)

Sutton, R. S., & Barto, A. G. 1998, Introduction to Reinforcement Learning, 1st edn. (Cambridge, MA, USA: MIT Press)

Takada, M., & Jain, B. 2004, MNRAS, 348, 897, doi: [10.1111/j.1365-2966.2004.07410.x](https://doi.org/10.1111/j.1365-2966.2004.07410.x)

Taylor, P. L., Bernardeau, F., & Huff, E. 2021, Phys. Rev. D, 103, 043531, doi: [10.1103/PhysRevD.103.043531](https://doi.org/10.1103/PhysRevD.103.043531)

Taylor, P. L., Bernardeau, F., & Kitching, T. D. 2018a, Phys. Rev. D, 98, 083514, doi: [10.1103/PhysRevD.98.083514](https://doi.org/10.1103/PhysRevD.98.083514)

Taylor, P. L., Kitching, T. D., & McEwen, J. D. 2018b, Phys. Rev. D, 98, 043532, doi: [10.1103/PhysRevD.98.043532](https://doi.org/10.1103/PhysRevD.98.043532)

Tegmark, M., Taylor, A. N., & Heavens, A. F. 1997, ApJ, 480, 22, doi: [10.1086/303939](https://doi.org/10.1086/303939)

Tikhonov, A. N., & Arsenin, V. Y. 1977, Solutions of Ill-posed problems (Winston)

Troxel, M. A., MacCrann, N., Zuntz, J., et al. 2018, PhRvD, 98, 043528, doi: [10.1103/PhysRevD.98.043528](https://doi.org/10.1103/PhysRevD.98.043528)

van Uitert, E., Joachimi, B., Joudaki, S., et al. 2018, MNRAS, 476, 4662, doi: [10.1093/mnras/sty551](https://doi.org/10.1093/mnras/sty551)

Wehrens, R., & Buydens, L. M. C. 2007, Journal of Statistical Software, 21, 1, doi: [10.18637/jss.v021.i05](https://doi.org/10.18637/jss.v021.i05)

Wehrens, R., & Kruisselbrink, J. 2018, Journal of Statistical Software, 87, 1, doi: [10.18637/jss.v087.i07](https://doi.org/10.18637/jss.v087.i07)

Wright, A. H., Hildebrandt, H., van den Busch, J. L., & Heymans, C. 2020a, A&A, 637, A100, doi: [10.1051/0004-6361/201936782](https://doi.org/10.1051/0004-6361/201936782)

Wright, A. H., Hildebrandt, H., van den Busch, J. L., et al. 2020b, A&A, 640, L14, doi: [10.1051/0004-6361/202038389](https://doi.org/10.1051/0004-6361/202038389)

Zuntz, J., Sheldon, E., Samuroff, S., et al. 2018, MNRAS, 481, 1149, doi: [10.1093/mnras/sty2219](https://doi.org/10.1093/mnras/sty2219)

APPENDIX

A. THEORY

In our metrics, the power spectrum between two tomographic bins i and j is computed using either the Core Cosmology Library (Chisari et al. 2019) or the JAX Cosmology Library (Lanusse & et al. 2021) as:

$$C_{\ell}^{ij} = \int_0^{\infty} \frac{q_i(\chi)q_j(\chi)}{\chi^2} P\left(\frac{\ell + \frac{1}{2}}{\chi}, \chi\right) d\chi \quad (\text{A1})$$

where $\chi = \chi(z)$ is the comoving distance and P the non-linear matter power spectrum at a fiducial cosmology. The kernel functions $q_i(\chi)$ are different for the lensing and clustering samples:

$$q_i^{\text{clust}}(\chi) = n_i(\chi) \quad (\text{A2})$$

$$q_i^{\text{lens}}(\chi) = \frac{3}{2} \Omega_m \left(\frac{H_0}{c}\right)^2 \frac{\chi}{a(\chi)} \int_{\chi}^{\infty} \frac{\chi' - \chi}{\chi'} n_i(\chi') d\chi' \quad (\text{A3})$$

where $n_i(\chi) = n_i(z) \frac{dz}{d\chi}$.

We evaluate these at 100 ℓ values from $\ell_{\min} = 100$ to $\ell_{\max} = 2000$.

We use a Gaussian estimate for the covariance (Takada & Jain 2004); this also incorporates the number of galaxies in the sample:

$$\text{Cov}(C_{\ell}^{ij}, C_{\ell}^{mn}) = \frac{1}{(2\ell+1)\Delta\ell f_{\text{sky}}} (D_{\ell}^{im} D_{\ell}^{jn} + D_{\ell}^{in} D_{\ell}^{jm}) \quad (\text{A4})$$

where $D_{\ell}^{ij} = C_{\ell}^{ij} + N_{\ell}^{ij}$, $\Delta\ell$ is the size in ℓ of the binned spectra, and we assume an $f_{\text{sky}} = 0.25$. The noise spectra are:

$$N_{\ell}^{\text{clust},ij} = \delta_{ij}/n_i \quad (\text{A5})$$

$$N_{\ell}^{\text{lens},ij} = \delta_{ij}\sigma_e^2/n_i \quad (\text{A6})$$

where n_i is the angular number density of galaxies in bin i (we assume equally weighted galaxies, and a total number density over all bins of 20 galaxies per square arcminute) and $\sigma_e = 0.26$, roughly matching that found in previous surveys (Troxel et al. 2018; Asgari et al. 2021; Hamana et al. 2020).

B. METHOD DETAILS

This appendix details the different methods submitted to the challenge.

Method implementations used in the challenge may be found in the GRAND-MERGE branch of the challenge repository http://github.com/LSSTDESC/tomo_challenge.

B.1. RANDOMFOREST

This method was submitted by the challenge organizers and used a random forest algorithm to assign galaxies.

Random forests (Breiman 2001) train a collection of individual *decision trees*, each of which consists of a set of bifurcating comparisons in which different features in the data (in this case, magnitudes and errors) are compared to criterion values to choose which branch to follow. Each “leaf” (end comparison) selects a classification bin for an input galaxy, and the tree is trained to choose comparison features and comparison values which maximize discrimination at each step and final leaf purity.

Since decision trees tend to over-fit, random forests generate a suite of trees, each randomly choosing a subset of features on which to train at each bifurcation. An average over the trained trees is taken as the overall classification.

In this implementation we chose nominal bin edges by splitting ensuring equal numbers of training set objects were in each bin, and then trained the forest to map magnitudes, magnitude errors, and galaxy sizes to bin indices. We use the SCIKIT-LEARN implementation of the random forest (Pedregosa et al. 2011).

B.2. LSTM

Methods B.2 - B.7 were submitted by a team of authors CRB, BF, GT, ESC, and EJG. All were built using TensorFlow and/or Keras, and chose bin edges such that an equal number of galaxies is assigned to each bin, and trained the network using the galaxies’ magnitudes and colours.

The LSTM method uses a Bidirectional Long Short Term Memory network to assign galaxies to redshift bins.

Recurrent Neural Networks (RNNs) (Schuster & Paliwal 1997; Medsker & Jain 1999; Pascanu et al. 2013) are a type of NN capable of analyzing sequential data, where data points have a strong correlation with their neighbours. Long Short Term Memory (LSTM) units are a particular type of RNN capable of retaining relevant information from previous points while at the same time removing unnecessary data. This is achieved through a series of gates with learnable weights connected to different activation functions to balance the amount of data retained or removed.

In some cases, relevant information can come both from data points coming before or after each point being analyzed. In such cases, two LSTMs can be combined,

each going in a different direction, to create effectively a bidirectional LSTM cell (Schuster & Paliwal 1997).

The Deep model is composed of a series of convolutional blocks (1d convolutional layer with a tanh activation followed by a MaxPooling layer) followed by a bidirectional LSTM layer and a series of fully connected layers.

B.3. AUTOKERAS LSTM

Autokeras (Jin et al. 2019) is an AutoML system based on Keras. Given a general neural network architecture and a dataset, it searches for the best possible detailed configuration for the problem at hand.

We started from the basic architecture and bin assignment scheme mentioned in Section B.2 and let Autokeras search for the configuration that results in the lowest validation loss. We kept the order of the layer blocks fixed, i.e., convolutional blocks, bidirectional LSTM, and dense blocks. We left the other hyperparameters free, such as the number of neurons, dropout rates, max-pooling layers, the number of convolutional filters, and strides.

A technical problem, involving conflicting versions of libraries and incompatible hardware, meant that this method could not be run in the final challenge.

B.4. LGBM

This method uses a Light Gradient Boosted Machine (LightGBM) (Ke et al. 2017) to assign galaxies to redshift bins.

LightGBM uses a histogram-based algorithm that assigns continuous feature values to discrete bins instead of other pre-sort-based algorithms for decision tree learning. LightGBM also grows the trees leaf-wise, which tends to achieve lower losses than level-wise tree growth. This method tends to overfit for small data so that a *max_depth* parameter can be specified to limit tree depth.

B.5. TCN

This method uses a Temporal-Convolutional network (TCN) (Bai et al. 2018) to assign galaxies to redshift bins.

Recurrent Neural Networks (such as LSTMs) are considered to be the state-of-the-art model for sequence modelling. However, research indicates that certain convolutional architectures can achieve human-level performance in these tasks (Dauphin et al. 2017).

TCNs are Fully Convolutional Networks with causal convolutions, in which the output at time t is convolved only with elements of time t and lower in the previous layer. This new approach prevents leakage of information from the future to the past. This simple model has

one disadvantage, in that it needs a very deep architecture or large filters to achieve a long history size.

By using dilated convolutions, where a fixed step is introduced between adjacent filter taps, the receptive field of the TCN can be increased without increasing the number of convolutional filters. Residual blocks (He et al. 2016) are also used to stabilize deeper and larger networks. These modifications cause TCNs to have a longer memory than traditional RNNs with the same capacity, and also require low memory for training.

We used the Keras implementation of TCN (Remy 2020) and chose bin edges such that an equal number of galaxies is assigned to each bin, and trained the network using the galaxies’ magnitudes and colours.

B.6. CNN

This method uses an optimized Convolutional Neural Network (CNN) to assign galaxies to redshift bins.

CNNs (LeCun et al. 2015) are layers inspired in pattern recognition types developed in mammals’ brains. They consist of kernels that are convolved with the data as it flows through the net. CNN-based models have emerged as state-of-the-art in several computer vision tasks, such as image classification and pose estimations, as well as having applicability in a range of different fields.

We combine the convolutional layers with dimensionality reduction (pooling layers) and different activation functions. Here, we used Autokeras to optimize a general convolutional architecture, using the galaxies’ magnitudes and colours to assign them to redshift bins, which were chosen such that an equal number of galaxies were assigned to each.

B.7. ENSEMBLE

This method combines different neural network architectures to assign galaxies to redshift bins.

Deep Ensemble models combine different neural network architectures to obtain better performance than any of the nets alone. In this method, we used the Bidirectional LSTM optimized by Autokeras, a ResNet (He et al. 2016) and a Fully Convolutional Network (FCN) (Long et al. 2015). The predictions of these models were averaged to get the final predicted bin.

B.8. SIMPLESOM

The SimpleSOM algorithm submitted by author AHW utilises a self-organising map (SOM, Kohonen 1982) to perform a discretisation of the high-dimensional colour-magnitude-space of the challenge training and reference datasets.

We utilise a branched version of the `kohonen`⁹ package (Wright et al. 2020b; Wehrens & Kruisselbrink 2018; Wehrens & Buydens 2007) within R (R Core Team 2015), which we integrate with the challenge’s python classes using the `rpy2` interface¹⁰. We train a 101×101 hexagonal-cell SOM with toroidal topology on the maximal combination of (non-repeated) colours, z -band magnitude, and so-called ‘band-triplets’. For example, for the ‘griz’ setup, our SOM is trained on the combination of z , $g-r$, $g-i$, $g-z$, $r-i$, $r-z$, $i-z$, $g-r-(r-i)$, $r-i-(i-z)$. This combination proved optimal during testing on the DC2 dataset, as determined by the 3x2pt SNR metric. The training and reference data then propagated into this trained SOM, producing like-for-like groupings between the two datasets. We then compute the mean redshift of the training sample sources within each cell and the number of reference sources per-cell. By rank-ordering the cells in mean training-sample redshift, we construct the cumulative distribution function of reference sample source counts, and split cells into n_{tomo} equal- N tomographic bins using this function.

In addition to this base functionality, the `SimpleSOM` method includes a mechanism for distilling N_{cell} SOM cells into $N_{\text{group}} < N_{\text{cell}}$ groups of cells, while maintaining optimal redshift resolution. This is done by invoking a hierarchical clustering of SOM cells (see Appendix B of Wright et al. 2020a), where in this case we combine cells based on the similarity of the cells’ $n(z)$ moments (mean, median, and normalized median absolute deviation from median) using complete-linkage clustering. The result of this procedure is the construction of fewer discrete groups of training and reference data, while not introducing pathological redshift-distribution broadening (as happens when, e.g., training using a lower resolution SOM and/or clustering cells based on distances in colour-magnitude space).

B.9. *PQNLD*

The ‘por que no los dos’ algorithm, submitted by author AHW, is a development of the `SimpleSOM` algorithm, adding the additional complexity of also computing template-based photometric redshift point-estimates using BPZ (Benítez 2000). Photo- z point-estimates are derived using the re-calibrated template set of Capak (2004) in combination with the Bayesian redshift prior from Raichoor et al. (2014), using only the (g)riz bands supplied in the challenge.

The algorithm seeks to leverage information from both template-based photometric redshift estimates and

machine-learning to improve the allocation of discretised cells in colour-magnitude-space to tomographic bins, by flagging and discarding sources which reside in cells that have significant colour-redshift degeneracies. In practice this is achieved by performing a quality-control step prior to the assignment of SOM cells to tomographic bins, whereby each cell i is flagged as having a catastrophic discrepancy between its mean training z and mean photo- z if:

$$\frac{|\langle z_{\text{train},i} \rangle - \langle z_{\text{phot},i} \rangle - \langle z_{\text{train}} - z_{\text{phot}} \rangle|}{\sigma_{[z_{\text{train}} - z_{\text{phot}}]}} \geq 5. \quad (\text{B7})$$

This flagging is inspired by similar quality control that is implemented in the redshift calibration procedure of Wright et al. (2020a), which removes pathological cells in the SOM prior to the construction of calibrated redshift distributions for KiDS. We note, though, that this procedure is unlikely to have a significant influence in this challenge, as it is primarily designed to identify and remove cells with considerable covariate shift between the training and reference samples; a problem which does not exist (by construction) in this challenge.

For a further discussion of the merits of band triplets in machine learning photo- z see Broussard & Gawiser (2021)

B.10. *COMPLEXSOM*

This method was submitted by authors DA, AHW, AN, EG, BA, and ABr.

The `ComplexSOM` method implements an additional optimization layer on the methodology used by `SimpleSOM`.

Let C_{ℓ}^{group} be the matrix containing all auto- and cross-power spectra between members of a large set of galaxy samples (called “groups” here). We can compress this large set into a smaller set of samples (called “bins” here), by combining different groups. Let A be the assignment matrix determining these bins, such that $A_{\alpha,i} = 1$ if group i is assigned to bin α , and 0 otherwise. In that case, the redshift distribution of bin α is given by $N_{\alpha}(z) = \sum_i A_{\alpha,i} n_i(z)$, where $n_i(z)$ is the redshift distribution of group i .

Defining the normalized assignment matrix B as

$$B_{\alpha,i} = A_{\alpha,i} \frac{\int dz n_i(z)}{\sum_j A_{\alpha,j} \int dz n_j(z)}, \quad (\text{B8})$$

C_{ℓ}^{group} is related to the matrix of cross-power spectra between pairs of bins via:

$$C_{\ell}^{\text{bin}} = B C_{\ell}^{\text{group}} B^T. \quad (\text{B9})$$

The rationale behind the `ComplexSOM` method is based on the observation that, while C_{ℓ}^{group} is a slow quantity to calculate for a large number of groups, B and

⁹ <https://github.com/AngusWright/kohonen.git>

¹⁰ <https://rpy2.github.io>

therefore C_ℓ^{bin} are very fast. Thus, given an initial set of groups characterizing the distribution of the full sample in colour space, C_ℓ^{group} can be precomputed once, and used to find the optimal assignment matrix B that maximizes the figure of merit in Equation 3, which can be written in terms of C_ℓ^{bin} alone as

$$F_{\theta\theta'} = \sum_\ell f_{\text{sky}} \frac{2\ell+1}{2} \text{Tr} [\partial_\theta C_\ell^{\text{bin}} (C_\ell^{\text{bin}})^{-1} \partial_{\theta'} C_\ell^{\text{bin}} (C_\ell^{\text{bin}})^{-1}]. \quad (\text{B10})$$

Note that the general problem of finding the matrix B that optimally compresses the information on a given parameter has an analytical solution in terms of Karhunen-Loeve eigenvectors (Tegmark et al. 1997). However, the assignment matrix used in this case has the additional constraints that it must be positive, discrete and binary (i.e. groups are either in a bin or they are not). Thus, finding the absolute maximum figure of merit would involve a brute-force evaluation of all matrix elements $A_{\alpha,j}$, which is an intractable $N_{\text{bin}}^{N_{\text{group}}}$ problem. We thus parametrize A in terms of a small set of continuous parameters, for which standard minimization routines can be used. In particular we use $N_{\text{bin}} - 1$ parameters, given by the edges of the redshift bins, and a group is assigned to a bin if its mean redshift falls within its edges. We also explored the possibility of ‘trashing’ groups if less than a fraction p_{in} of its redshift distribution fell within its preassigned bin, treating p_{in} as an additional free parameter. We found that adding this extra freedom did not translate into a significant improvement in the final level of data compression.

Once the SOM has been generated, the `ComplexSOM` method proceeds as follows. First, the full SOM is distilled into a smaller set of $\mathcal{O}(100)$ groups based by combining SOM cells with similar moments of their redshift distributions, thus ensuring that this process does not induce any catastrophic $N(z)$ broadening. The large C_ℓ^{group} is then precomputed for the initial set of groups. Finally, we find the optimal assignment matrix, defined in terms of the free redshift-edge parameters, by maximizing the figure of merit in Eq. B10 using Powell’s minimization method (Powell 1964).

B.11. UTOPIA

The ‘Unreliable Technique that OutPerforms Intelligent Alternatives’ is a method submitted by AHW that is designed, primarily, as a demonstration of the care that must be taken in the interpretation of the tomographic challenge results. The method performs the simplest-possible direct mapping between the training and reference data, by performing a nearest-neighbour assignment of training sample galaxies to each reference

sample source in n_{band} magnitude-only space. Each reference sample galaxy is then assigned the redshift of its matching training-sample source, and these redshifts are used to bin the reference galaxies into n_{tomo} equal- N tomographic bins. Importantly, the method was specifically implemented so as to use only the minimum information contained within the available bands (by using magnitudes alone, without any colours, etc.).

In this way UTOPIA is the simplest possible algorithm (utilising all available photometric bands) that one can implement for tomography. It is also a method whose performance is optimal in the limit of an infinitely large, perfectly representative training sample; i.e. the limit in which this challenge operates. As the requirements of perfect training-sample representativity and large size are violated, UTOPIA ought to assign redshifts to reference galaxies from increasingly distant regions of the multi-dimensional magnitude-space, resulting in poorer (i.e. unreliable) tomographic binning. Therefore, UTOPIA acts as a warning against over-interpretation of the tomographic challenge results, as success in the challenge need not translate to optimal-performance/usefulness under realistic survey conditions. Instead, the challenge results should be interpreted holistically, by comparing the performance between different classes of methods, rather than individuals. The authors have endeavoured to do so in the conclusions presented here.

B.12. GPzBINNING

This method was submitted by author PH.

GPzBin is based on GPz (Almosallam et al. 2016b,a), a machine learning regression algorithm originally developed for calculating the photometric redshifts of galaxies (Gomes et al. 2018; Duncan et al. 2018; Hatfield et al. 2020) but now also applied to other problems in physics (Peng & Bai 2019; Hatfield et al. 2020). The algorithm is based on a Gaussian Process (GP; essentially an un-parametrised continuous function defined everywhere with Gaussian uncertainties); GPz specifically uses a sparse GP framework, a fast and a scalable approximation of a full process (Rasmussen & Williams 2005).

The mean $\mu(x)$ and variance $\sigma(x)^2$ for predictions as a function of the input parameters x (typically the photometry) are both linear combinations of a finite number of ‘basis functions’: multi-variate Gaussian kernels with associated weights, locations and covariances. The algorithm seeks to find the optimal parameters of the basis functions such that the mean and variance functions are the most likely functions to have generated the data. The key innovations introduced by GPz include

a) input-dependent variance estimations (heteroscedastic noise), b) a ‘cost-sensitive learning’ framework where the algorithm can be tailored for the precise science goal, and c) properly accounting for uncertainty contributions from both variance in the data (β_\star^{-1}) as well as uncertainty from lack of data (ν) in a given part of parameter space (by marginalising over the functions supported by the GP that could have produced the data).

GPzBin is a simple extension to GPz for the problem of tomographic binning. For a given number of tomographic bins it selects redshift bin edges z_i such that there are an equal number of training galaxies in each bin. Testing sample galaxies are then assigned to the bin corresponding to their GPz predicted photometric redshift. The code allows for two selection criteria for removing galaxies for which it was not possible to make a good photometric redshift prediction: 1) cutting galaxies close to the boundaries of bins based on an ‘edge strictness’ parameter U which removes galaxies where $\mu \pm U \times \sigma \leq z_i$ and 2) cutting galaxies based on the degree E to which GPz is having to extrapolate to make the redshift prediction, removing galaxies with $\nu > E\sigma^2$ (see Figure 12 of Hatfield et al. 2020). Cutting galaxies removes some signal at the possible benefit of improving binning purity. As the training and test data were sampled from the same distribution in this data challenge we might not expect removing galaxies to give huge improvements in binning quality, but cuts based on E and U might become more useful in future studies where the training and test data have substantially different colour-magnitude distributions.

We used these settings in GPz for this challenge (see Almosallam et al. 2016b,a for definitions): x=100, maxIter=500, maxAttempts= 50, method=GPVC, normalize=True, and joint=True.

B.13. JAXCNN & JAXRESNET

This method was submitted by the author AP.

JaxCNN and JaxResNet are convolutional neural network based algorithms that map the relationship between the colour-magnitude data of galaxies to their bin indices. Convolutional neural network (CNN) models, as described in section B.6, consist of several layers, each consisting of a linear convolution operator followed by polling layers and a nonlinear activation function. Residual Network (ResNet) models take one step further and learn the *identity* mapping by skipping, or adding *shortcut* connections to, one or more layers (He et al. 2016). ResNet helps solve the vanishing gradient problem, allowing a deeper neural network.

JaxCNN uses 2-layer convolutional neural networks and JaxResNet uses a stack of 3 layers consisting of

$1 \times 1, 3 \times 3$, and 1×1 convolutions with shortcut connections added to each stack. Both methods use the Rectified Linear Unit (ReLU) activation function under the ADAM optimizer Kingma & Ba (2014) with a learning rate of 0.001.

We chose the learning algorithm for both methods to minimize the reciprocal of the figure of merit F , where F is defined in Equation 3. We implement these models using the JAX-based Flax neural network library Bradbury et al. (2018).

B.14. NEURALNETWORK 1 & 2

This method was submitted by the author FL.

The NEURALNETWORK approach combines the two following ideas:

- Using a simple neural network to parameterize a bin assignment function f_θ taking available photometry as the input and returning a bin number.
- Optimizing the parameters of f_θ as to maximize a target score, either the total SNR (Equation 1), or the DETF FoM (Equation 3).

The method directly solves the problem of optimal bin assignment given available photometry, to maximize the cosmological information, without estimating a redshift.

Details of the particular neural network are mostly irrelevant; the main difficulty in this approach is to be able to compute the back-propagation of gradients through the cosmological loss function to update the parameters θ of the bin assignment function. This is was made possible for this challenge by the JAX-COSMO library (Lanusse & et al. 2021), which allows the computation of both metrics using the JAX automatic differentiation framework (Bradbury et al. 2018).

In practice, to parameterize f_θ we use a simple dense neural network, composed of 3 linear layers of size 500 with leaky_relu activation function and output batch normalization. The last layer of the model is a linear layer with an output size matching the number of bins, and softmax activation. We implement this model using the JAX-based FLAX neural network library (Heek et al. 2020).

Training is performed using batches of 5000 galaxies, over 2000 iterations under the ADAM optimizer (Kingma & Ba 2014) with a base learning rate of 0.001. The loss functions \mathcal{L} used for training directly derive from the challenge metrics, and constitute the only difference between the NeuralNetwork 1 & NeuralNetwork 2 entries:

- NeuralNetwork 1: $\mathcal{L}_1 = 1/S_{FoM}$
- NeuralNetwork 2: $\mathcal{L}_2 = -S_{SNR}$

B.15. PCACLUSTER

This entry was submitted by author DG.

Principal Component Analysis (PCA) reduces the dimensionality of a dataset by calculating eigenvectors that align with the principal axes of variation in the data (Jolliffe & Cadima 2016). PCACLUSTER uses PCA to reduce the flux & colour data set to three dimensions.

To generate the PCA dimensions used by this method the PCA algorithm takes in the r -band flux and ri and iz colours and outputs three principal components. If the data set provides the g -band, the algorithm also uses the gr colour when determining eigenvectors. Tomographic bins are then determined in this three dimensional space using a clustering algorithm where each observation is assigned to a bin by determining which cluster centroid is closest to that observation.

In order to determine optimal centroid positions, clustering is framed as a gradient descent problem that seeks to maximize the requested metric: either the SNR or the FoM. This approach of identifying clusters using gradient descent is inspired by the similar approach to K-means clustering in Bottou & Bengio (1995).

This entry uses JAX_COSMO to take the derivative of the requested metric and classification function combination with respect to the centroid locations to calculate gradients and weight updates (Lanusse & et al. 2021). The speed of training PCACLUSTER is directly proportional to the number of requested centroids (the number of requested tomographic bins) and the amount of training data used.

B.16. ZOTBIN AND ZOTNET

This pair of related methods was submitted by author DPK and its associated code is available at <https://github.com/dkirkby/zotbin>.

The ZotBin method consists of three stages: preprocessing, grouping, and bin optimization. The ZotNet method uses the same preprocessing, then skips directly to bin optimization. Both methods optimize the final bins to maximize an arbitrary linear combination of the three metrics defined in 3.3, using the JAX library Bradbury et al. (2018) for efficient computation. The goal of ZotNet is to find a nearly optimal set of bins (for a specified linear combination of metrics) using a neural network, at the expense of interpretability of the results. The ZotBin method aims to perform almost as well as ZotNet, but with a much more interpretable mapping from input features to final bins.

Both methods transform the n input fluxes into $n-1$ colours and one flux. The data are very sparse in this n -dimensional feature space and exhibit complex correlations. The preprocessing step transforms to a new n

dimensional space where the data is nearly uncorrelated and dense on the unit hypercube $[0, 1]^n$. This is accomplished by learning a normalizing flow Papamakarios et al. (2019) that maps the complex input probability density into a multivariate unit Gaussian, then applying the error function to yield a uniform distribution. Although the resulting transformation is non-linear, it is invertible and differentiable, and thus provides an interpretable smooth mapping.

The second stage of ZotBin starts by dividing the unit hypercube $[0, 1]^n$ from the preprocessing step into a regular lattice of $\mathcal{O}(10K)$ cells which, by construction, each contain a similar number of training samples. Next, adjacent cells are iteratively merged into $M \sim 100$ groups of cells by combining at each step the pair of groups that are most “similar”. We define similarity as the product of similarities in feature and redshift space. Redshift similarity is based on the histogram of redshifts associated with each group, interpreted as a vector.

The final stage of ZotBin selects linear combinations of the M groups to form the N output bins. This is accomplished by optimizing the specified metric combination with respect to the $M \times N$ matrix of linear weights.

The ZotBin method defines a fully invertible sequence of steps that transform the input feature space into the final bins, so that each bin is associated with a well-defined region in colour / flux space. The ZotNet method, on the other hand, trains a neural network to directly map from the preprocessed unit hypercube $[0, 1]^n$ into N output bins by optimizing the specified metric combination. The resulting map is not invertible, so less interpretable, but also less constrained than ZotBin, so expected to achieve somewhat better performance.

B.17. FUNBINS

This entry was submitted by author ABa.

This method uses the random forest algorithm described in section B.1 to assign galaxies to tomographic bins, but modifies the target bin edge selection method. There are 3 options for determining the edges used to assign labels to the training data: *log*, *random*, and *chi*.

The first option, *log*, calculates bin edges such that the number of galaxies in each bin grows logarithmically instead of being constant as in section B.1. This option uses increasingly large bins for more distant galaxies and tests the relative importance of nearby galaxies.

The second option, *random*, draws the intermediate bin edges from a uniform distribution while fixing the outer edges to the limits of the data. This option is not theoretically motivated and designed only to study the sensitivity to the binning.

The last option, *chi*, calculates redshift bin edges whose corresponding comoving distances are equally spaced, using Planck15 (Planck Collaboration et al. 2016) cosmology for the distance-redshift relationship. This should lead to roughly equal shot noise for the angular power in each bin. This method was used in the scores shown in this paper.

Once the bin edges are determined by either of the methods above, the random forest is trained as described in section B.1.

B.18. FFNN

This entry was submitted by author EN.

The method is a Feed Forward Neural Network (FFNN), a classic type of neural network. This implementation used the Keras API in the TensorFlow library. Three components, a flattener, and two dense layers of ReLu neurons, were optimized by ADAM on the sparse categorical cross-entropy of the classifications. A StandardScaler was used to pre-process the data, and the training stopped when there was no improvement in the validation loss for three consecutive epochs, to avoid overfitting.

The network is trained using the galaxies' magnitudes, colours and band-triplets as well as their errors to assign them to the redshift bins. Prior to processing the training and validation data, the non-detection placeholder magnitudes (30.0) were replaced with an approximation of the 1σ detection limit as an estimate for the sky noise threshold, where Signal to Noise ratio, S/N, equals 1. We first compute the error equivalent of $dm = 2.5\log(1+N/S)$ where $dm \sim 0.7526$ magnitudes for $N/S = 1$, and then fit a logarithmic model to the magnitude as a function of its error for different bands in the training data. This gives us the magnitude corresponding to this limit and in order to be consistent we use this value along with its error to replace the non-detections everywhere during the process.

B.19. MLPQNA

This entry was submitted by authors SC and MB.

The Multi Layer Perceptron trained by Quasi Newton Algorithm (MLPQNA; Brescia et al. 2012), is a feed-forward neural network for multi-class classification and single/multi regression use cases.

The architecture is a classical Multi Layer Perceptron (MLP; Rosenblatt 1961) with one or more hidden layers, on which the supervised learning paradigm is run using the Quasi Newton Algorithm (QNA), implemented through the L-BFGS rule (Nocedal 1980). L-BFGS is a solver that approximates the Hessian matrix, representing the second-order partial derivative of a function.

Further, it approximates the inverse of the Hessian matrix to perform parameter updates. MLPQNA uses the least square loss function with the Tikhonov regularization (Tikhonov & Arsenin 1977) for regression. It uses the cross-entropy (de Boer et al. 2005) and softmax (Sutton & Barto 1998) as output error evaluation criteria for classification.

Besides several scientific contexts and projects in which MLPQNA has successfully been used, it was recently used as the kernel embedded into the method METAPHOR (Cavuoti et al. 2016) for photo-z estimation, which participated in the LSST Photometric Redshift PDF Challenge (Schmidt et al. 2020b).

The MLPQNA python implementation used here uses a customized Scipy version of the L-BFGS built-in rule. It used two hidden layers with $2N - 1$ and $N + 1$ nodes respectively, where N is the number of input features (depending on the experiment). The decay was set to 0.1.

B.20. STACKED GENERALIZATION

This method was submitted by author JEC.

Stacked generalization consists of stacking the output of several individual estimators and using a classifier to compute the final prediction. Stacking methods use the strength of each individual estimator by using their outputs as input of a final estimator. This entry stacked *Gradient Boosted Trees* (GBT) classifiers with standard Random Forests (RFs), and then used a Logistic Regression as the final step.

GBT is a machine learning method which combines decision trees (like the standard RF) by performing a weighted mean average of individual trees (Friedman 2002; Hastie et al. 2009). The prediction $F(X)$ of the ensemble of trees for a new sample X is given by

$$F(X) = \sum_k w_k F_k(X) \quad (B11)$$

where $F_k(X)$ is the individual tree answer and w_k a weight per tree. Unlike the RF, the tree depth is rather small and the training of the k -th tree is based on the errors of the $(k-1)$ -th tree. Like the RF, a randomly chosen fraction of features ($\approx 50\%$) is omitted at each split, and this step is changed at each tree (leading to a Stochastic Gradient Descent algorithm). GBT learning is essentially non-parallelizable and so cannot use a map-reduce paradigm, unlike RF. It suffers from the opposite problem to RF's overfitting, and is subject to high bias, so one generally combines many weak individual learners.

The two methods have their own systematics; they notably differ in the feature importances. Stacking the two is therefore especially effective. The submitted method

combined 50 GBTs with 50 RFs using the SKLEARN STACKINGCLASSIFIER.

An iterative procedure was used to progressively change the target bin edges to optimize one of the metrics (FOMs or SNRs) between the trainings of the classifiers. In general, we recover different choices for each statistic, but the differences are relatively marginal. This procedure was done by hand for this challenge, but could be automated and applied to any kind of classifier.

Although this entry stacked GBTs and RFs, the same approach can be used more generally, such as using one classifier optimized for high redshift and another for low, or one classifier for an SNR metric and a second for an FOM metric. This makes stacking approaches particularly flexible.

C. MISTAKES

The challenge organizers made a number of mistakes when building and running the challenge. These do not invalidate our process or results, but we describe some of them here in the hope of being useful for future challenge designers.

C.1. *Splitting nominal bin choice from assignment*

As noted in the main test, there were two ways to obtain good scores in the challenge: either a team could choose the best nominal bin edges, or find the best method to put galaxies into those bins once they are chosen. These two are not completely disconnected: some theoretically powerful choices of nominal edges could prove impossible to assign in practice. But it would still have been useful to separate the challenge into two separate parts, fixing the edges while optimizing classifiers, and vice versa. We can retrospectively determine this since we understand the classifiers, but the picture would have been clearer doing so in advance.

C.2. *Infrastructure*

Since submissions could use a wide variety of libraries and dependencies, it was extremely difficult after the challenge was complete to build appropriate environments for all the challenges in order to run the methods on additional data sets. In retrospect, a robust and careful continuous integration tool with a mechanism for entrants to specify an environment (for example, a container or a CONDA requirements file) could have been used to simplify this and ensure all methods could be easily run by the organizers.

One additional issue, though, was that many methods required GPUs to train in a reasonable time, and specifying an environment on these systems can be more complicated.

C.3. *Guidance on caching & batch processing*

Since the training process for the challenge could be slow for some algorithms, many entries (very reasonably) cached trained models or other values for later use. In some cases these cached values were then incorrectly picked up by subsequent runs on new data sets, leading to (at best) crashes and at worst silently poor scores. We should have provided an explicit caching mechanism for entrants to avoid such issues.

Additionally, the challenge supplied the data described in Section 3.2 to entrants, and some assumed that it was safe to hard-code specific paths to them or otherwise assume fixed data inputs. This led to problems when switching to new test data sets. Again, a requirement enforced by continuous integration could have checked this.

D. NORMALIZED METRIC SCORES

Figures 10, 11, and 12 show metric scores normalized between random assignment and perfect assignment to equal number density bins for CosmoDC2/riz, Buzzard/griz and Buzzard/riz respectively:

$$S_{\text{norm}} = \frac{S - S_{\text{random}}}{S_{\text{perfect,eq}} - S_{\text{random}}} \quad (\text{D12})$$

E. FULL 9-BIN RESULTS TABLES

Tables 3 and 4 show all calculated metrics when generating nine tomographic bins for CosmoDC2 and Buzzard respectively. The *ww* columns show weak-lensing metrics, *gg* show galaxy clustering, and *3x* the full 3x2pt metric. Methods above the horizontal line trained bin edges; methods below used fixed fiducial ones, though in some cases did some hand-tuning of them before submission. In each section the highest scoring method is highlighted.

As in table 2, some values are missing due to failure or time-out of the method (*) or pathological bin assignments (-). Failure rates were higher for the 9-bin runs than for the lower bin counts.

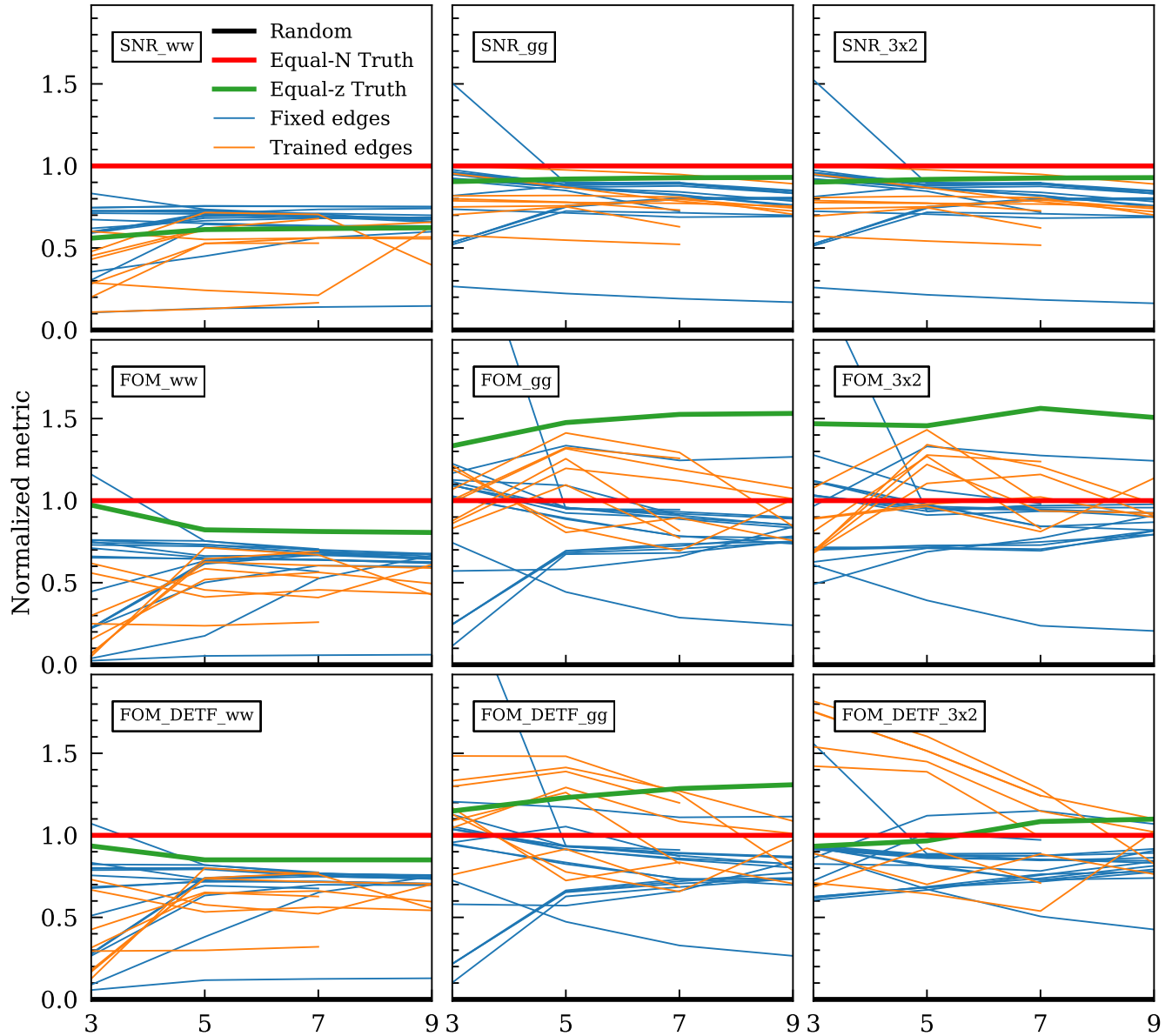


Figure 10. Normalized scores for each method, following the scheme of Figure 9 but for CosmoDC2 with riz bands

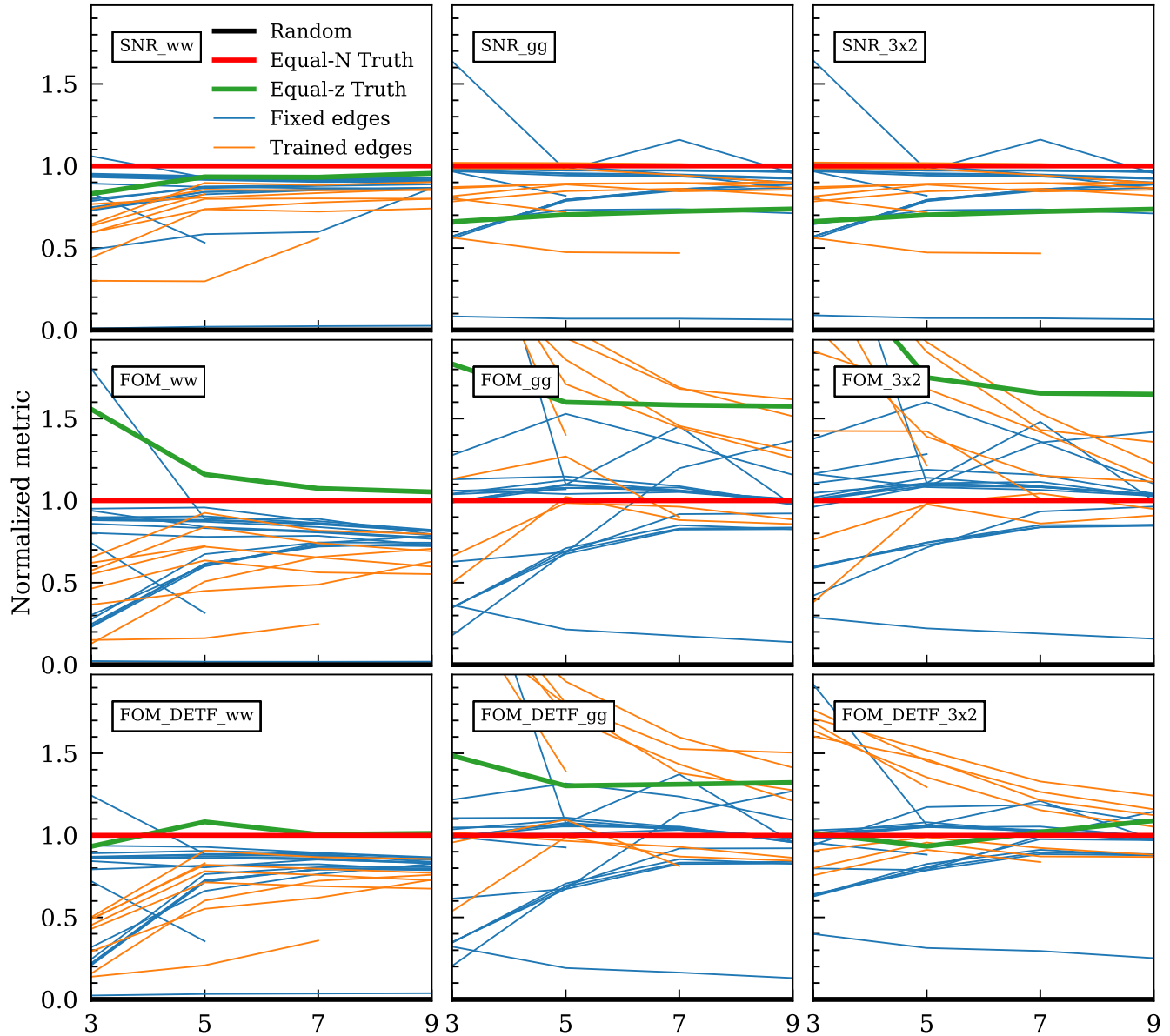


Figure 11. Normalized scores for each method, following the scheme of Figure 9 but for Buzzard with griz bands

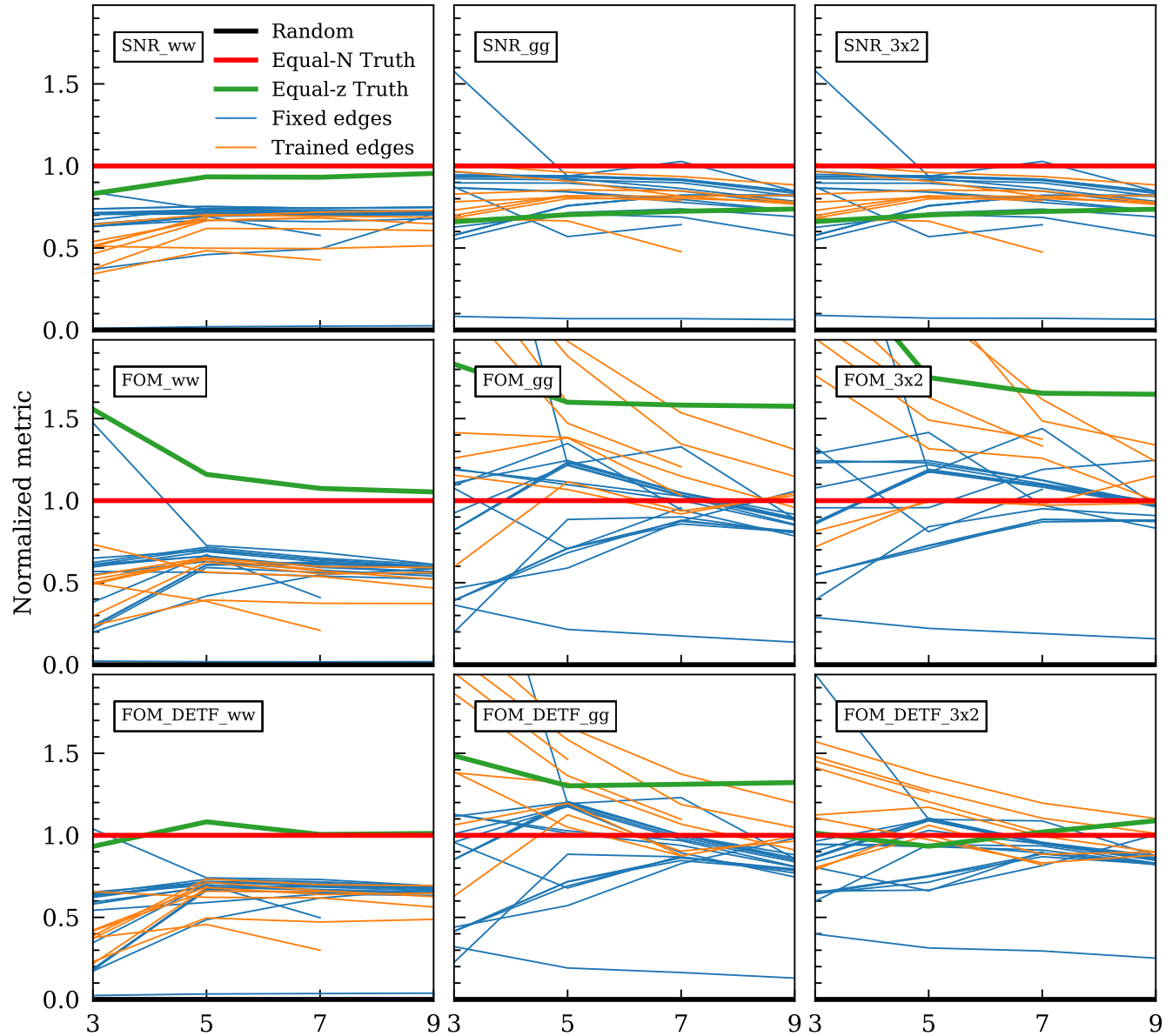


Figure 12. Normalized scores for each method, following the scheme of Figure 9 but for Buzzard with riz bands

Table 3. The 9-bin results for all metrics calculated for all methods on the CosmoDC2 sample.

Method	riz						griz					
	SNR			$\sigma_8 - \Omega_m$ FOM			SNR			$\sigma_8 - \Omega_m$ FOM		
	ww	gg	3x	ww	gg	3x	ww	gg	3x	ww	gg	3x
COMPLEXSOM	349.5	1538.1	1540.0	25.4	1830.7	7919.6	0.7	16.2	101.6	348.1	1556.5	1558.1
JAXCNN	—	—	—	—	—	—	—	—	—	—	—	—
JAXRESNET	—	—	—	—	—	—	—	—	—	—	—	—
NEURALNETWORK1	342.1	1513.0	1515.6	25.0	2043.7	8666.6	0.7	18.1	109.9	340.6	1468.6	1471.5
NEURALNETWORK2	353.1	1742.6	1744.2	35.8	2440.7	10025.7	0.9	22.4	136.1	350.4	1841.7	1842.9
PCACLUSTER	*	*	*	*	*	*	*	*	*	*	*	*
ZOTBIN	350.0	1560.2	1562.2	29.1	2449.1	8013.3	0.7	23.3	135.3	357.9	1740.5	1741.8
ZOTNET	354.3	1574.0	1575.8	34.6	2604.4	8150.8	0.9	25.0	145.9	363.1	1732.6	1733.9
AUTOKERAS_LSTM	—	—	—	—	—	—	—	—	—	364.3	1659.1	1660.7
CNN	354.5	1628.9	1630.5	38.1	1808.9	7000.4	0.9	16.9	103.3	366.0	1731.1	1732.3
ENSEMBLE1	*	*	*	*	*	*	*	*	*	*	*	*
FUNBINS	355.7	1497.2	1499.2	39.8	3068.2	10959.1	0.9	25.6	141.8	367.9	1658.3	1659.7
GPzBINNING	358.2	1505.4	1507.4	35.1	1825.8	7197.6	0.9	16.9	111.7	366.5	1700.7	1701.9
IBANDONLY	330.3	854.7	866.6	3.6	583.1	1829.9	0.2	6.1	57.3	330.3	854.7	866.6
LGBM	356.3	1638.9	1640.5	39.6	1896.2	7215.1	0.9	17.8	108.2	365.8	1734.4	1735.6
LSTM	354.2	1629.1	1630.8	38.2	1818.0	7008.3	0.9	17.0	103.6	366.1	1729.3	1730.5
MLPQNA	355.1	1674.8	1676.5	38.0	2177.1	8624.5	0.9	20.0	121.8	367.5	1809.2	1810.4
STACKED GENERALIZATION	351.6	1670.1	1672.2	39.1	2036.3	8038.7	0.9	19.3	120.4	358.8	1837.8	1839.4
PQNLD	358.7	1583.4	1585.1	36.4	1869.4	7666.6	0.9	16.8	105.4	368.2	1801.3	1802.5
RANDOM	323.5	646.3	670.1	0.0	0.6	17.7	0.0	0.0	1.2	323.5	646.3	670.1
RANDOMFOREST	355.6	1687.5	1689.2	39.6	2156.0	8447.7	0.9	19.9	118.5	368.1	1823.9	1825.1
SIMPLESOM	358.7	1572.8	1574.4	36.7	1785.8	7244.5	0.9	16.0	98.5	36.4	1788.5	1789.7
FFNN	355.2	1671.3	1673.0	37.7	2064.0	8170.0	0.9	19.0	114.7	367.3	1798.6	1799.8
TCN	355.3	1693.1	1694.7	38.7	2055.4	7955.5	0.9	18.9	110.5	366.2	1814.3	1815.5
UTOPIA	353.2	1612.4	1614.4	36.3	2022.5	8148.8	0.9	18.5	112.2	367.6	1807.4	1808.6

Table 4. The 9-bin results for all the metrics calculated for all methods on the Buzzard sample.

Method	riz									griz								
	SNR			$\sigma_8 - \Omega_m$ FOM			$w_0 - w_a$ FOM			SNR			$\sigma_8 - \Omega_m$ FOM			$w_0 - w_a$ FOM		
	ww	gg	3x	ww	gg	3x	ww	gg	3x	ww	gg	3x	ww	gg	3x	ww	gg	3x
COMPLEXSOM	243.9	1659.7	1660.1	8.4	1728.2	5372.0	0.4	16.5	74.9	256.3	1826.0	1826.4	15.9	1462.7	5177.9	0.6	14.3	75.0
JAXCNN	—	—	—	—	—	—	—	—	—	258.6	1830.2	1830.5	15.5	2152.7	6143.8	0.6	21.2	95.4
JAXRESNET	—	—	—	—	—	—	—	—	—	—	—	—	—	—	—	—	—	—
NEURALNETWORK1	253.2	1729.1	1729.5	13.3	2168.6	7304.1	0.5	19.9	93.7	260.7	1773.2	1773.5	17.9	2502.8	7405.5	0.6	23.4	105.4
NEURALNETWORK2	251.5	1810.4	1810.9	12.6	1705.4	6279.2	0.5	16.0	76.5	258.9	1948.7	1949.0	14.1	1417.1	4962.9	0.5	14.0	73.9
PCACLUSTER	*	*	*	*	*	*	*	*	*	*	*	*	*	*	*	*	*	*
ZOTBIN	247.9	1674.3	1674.9	10.5	1584.9	5448.1	0.4	15.1	76.5	253.7	1787.2	1787.6	12.4	2084.0	6086.2	0.5	20.1	89.4
ZOTNET	249.7	1673.3	1673.9	11.7	1897.9	6755.9	0.5	17.4	86.0	256.3	1727.2	1727.6	13.4	2672.5	6686.8	0.5	25.0	98.4
AUTOKERAS_LSTM	—	—	—	—	—	—	—	—	—	255.4	1844.6	1845.0	11.5	1499.6	5123.5	0.5	14.4	72.2
CNN	252.2	1724.5	1725.0	13.2	1335.4	4789.3	0.5	13.1	70.3	259.0	1814.3	1814.6	16.2	1364.9	4641.3	0.6	13.7	74.5
ENSEMBLE1	253.1	1761.4	1761.9	13.7	1470.2	5293.3	0.5	14.2	74.6	261.1	1901.2	1901.5	17.9	1609.7	5443.5	0.6	15.9	82.9
FUNBINS	251.1	1412.5	1413.1	11.8	1297.3	4542.4	0.5	12.4	72.2	260.1	1588.2	1588.6	17.4	1913.5	6017.6	0.6	18.1	91.7
GPzBINNING	254.1	1561.6	1562.1	12.5	1328.6	4958.8	0.5	12.8	70.7	260.7	1788.9	1789.2	16.7	1524.0	5261.6	0.6	15.3	82.5
IBANDONLY	222.7	755.5	763.7	0.4	227.8	867.6	0.0	2.2	22.0	222.7	755.5	763.7	0.4	227.8	867.6	0.0	2.2	22.0
LGBM	252.5	1732.6	1733.0	13.4	1345.8	4807.2	0.5	13.2	70.7	259.2	1814.6	1814.9	16.5	1382.5	4658.0	0.6	13.9	75.4
LSTM	252.3	1724.0	1724.5	13.3	1330.7	4764.1	0.5	13.0	69.9	259.2	1815.0	1815.3	16.5	1366.0	4620.1	0.6	13.8	74.7
MLPQNA	252.9	1757.1	1757.6	13.7	1479.6	5300.1	0.5	14.3	73.2	261.3	1917.1	1917.4	18.3	1659.0	5637.5	0.6	16.4	83.4
STACKED GENERALIZATION	252.3	1682.0	1682.6	13.1	1748.2	6796.2	0.5	16.3	85.3	259.1	1779.7	1780.1	17.6	2254.6	7736.9	0.6	21.1	97.2
PQNLD	254.1	1609.2	1609.6	12.7	1406.6	5281.2	0.5	13.4	70.6	261.8	1858.2	1858.5	18.3	1611.9	5593.7	0.6	15.9	84.3
RANDOM	221.5	674.0	680.5	0.0	0.4	6.3	0.0	0.8	221.5	674.0	680.5	0.0	0.4	6.3	0.0	0.0	0.8	
RANDOMFOREST	252.1	1721.9	1722.5	13.1	1462.0	5272.6	0.5	14.1	72.5	261.3	1913.0	1913.3	18.2	1658.2	5647.6	0.6	16.3	83.5
SIMPLESOM	254.0	1608.6	1609.1	12.7	1415.2	5352.9	0.5	13.5	70.7	261.8	1830.6	1830.9	18.5	1622.2	5685.9	0.6	15.9	84.7
FFNN	252.6	1744.7	1745.2	13.5	1465.8	5251.9	0.5	14.1	72.4	260.8	1910.9	1911.2	17.7	1668.3	5677.1	0.6	16.4	83.5
TCN	252.3	1761.4	1762.0	13.4	1514.0	5414.2	0.5	14.6	74.6	259.1	1913.4	1913.7	16.4	1651.7	5613.3	0.6	16.3	82.4
UTOPIA	252.1	1658.9	1659.3	12.1	1457.9	5354.9	0.5	13.9	73.6	261.2	1865.4	1865.7	17.2	1632.7	5637.6	0.6	16.0	83.1